Selective glutamine metabolism inhibition in tumor cells improves anti-tumor T lymphocyte activity in triple-negative breast cancer

Deanna N. Edwards, … , Mark R. Boothby, Jin Chen

Research In-Press Preview Oncology

Rapidly proliferating tumor and immune cells need metabolic programs that support energy and biomass production. The amino acid glutamine is consumed by effector T cells and glutamine-addicted triple-negative breast cancer (TNBC) cells, suggesting that a metabolic competition for glutamine may exist within the tumor microenvironment, potentially serving as a therapeutic intervention strategy. Here, we report that there is an inverse correlation between glutamine metabolic genes and markers of T cell-mediated cytotoxicity in human basal-like breast cancer (BLBC) patient datasets, with increased glutamine metabolism and decreased T cell cytotoxicity associated with poor survival. We found that tumor cell-specific loss of glutaminase (GLS), a key enzyme for glutamine metabolism, improved anti-tumor T cell activation in both a spontaneous mouse TNBC model and orthotopic grafts. The glutamine transporter inhibitor V-9302 selectively blocked glutamine uptake by TNBC cells but not CD8$^+$ T cells, driving synthesis of GSH, a major cellular antioxidant, to improve CD8$^+$ T cell effector function. We propose a "glutamine steal" scenario, in which cancer cells deprive tumor-infiltrating lymphocytes of needed glutamine, thus impairing anti-tumor immune responses. Therefore, tumor-selective targeting of glutamine metabolism may be a promising therapeutic strategy in TNBC.

Find the latest version:

Selective glutamine metabolism inhibition in tumor cells improves anti-tumor T lymphocyte activity in triple-negative breast cancer

Deanna N. Edwards[1], Verra M. Ngwa[2], Ariel L. Raybuck[3], Shan Wang[1], Yoonha Hwang[1], Laura C. Kim[2], Sung Hoon Cho[3], Yeeun Paik[3], Qingfei Wang[4,5], Siyuan Zhang[4,5], H. Charles Manning[6,7,8,9,10], Jeffrey C. Rathmell[3,10], Rebecca S. Cook[2,10,11], Mark R. Boothby[1,2,3,12], and Jin Chen[1,2,10,11,12,13]*

[1]Division of Rheumatology and Immunology, Department of Medicine, Vanderbilt University Medical Center, Nashville, Tennessee, USA.
[2]Program in Cancer Biology, Vanderbilt University, Nashville, Tennessee, USA.
[3]Department of Pathology, Microbiology and Immunology, Vanderbilt University Medical Center, Nashville, Tennessee, USA.
[4]Department of Biological Sciences, College of Science, University of Notre Dame, Notre Dame, Indiana, USA.
[5]Mike and Josie Harper Cancer Research Insititute, University of Notre Dame, South Bend, Indiana, USA.
[6]Department of Chemistry, Vanderbilt University, Nashville, Tennessee, USA.
[7]Center for Molecular Probes, Vanderbilt University Medical Center, Nashville, Tennessee, USA.
[8]Vanderbilt Institute for Imaging Sciences, Vanderbilt University Medical Center, Nashville, Tennessee, USA.
[9]Department of Radiology and Radiological Sciences, Vanderbilt University Medical Center, Nashville, Tennessee, USA.
[10]Vanderbilt-Ingram Cancer Center, Vanderbilt University Medical Center, Nashville, Tennessee, USA.
[11]Department of Cell and Developmental Biology, Vanderbilt University, Nashville, Tennessee, USA.
[12]Vanderbilt Institute for Infection, Immunology and Inflammation, Vanderbilt University Medical Center, Nashville, Tennessee, USA.
[13]Veterans Affairs Medical Center, Tennessee Valley Healthcare System, Nashville, Tennessee, USA.

*Correspondence should be addressed to:
Jin Chen, M.D., Ph.D.
Professor of Medicine
T-3207E, MCN
Vanderbilt University Medical Center
Nashville, TN 37232
Email: jin.chen@vanderbilt.edu
Tel. 615-343-3819
Conflict of Interest Statement: The authors have declared that no conflict of interest exists.

Abstract

Rapidly proliferating tumor and immune cells need metabolic programs that support energy and biomass production. The amino acid glutamine is consumed by effector T cells and glutamine-addicted triple-negative breast cancer (TNBC) cells, suggesting that a metabolic competition for glutamine may exist within the tumor microenvironment, potentially serving as a therapeutic intervention strategy. Here, we report that there is an inverse correlation between glutamine metabolic genes and markers of T cell-mediated cytotoxicity in human basal-like breast cancer (BLBC) patient datasets, with increased glutamine metabolism and decreased T cell cytotoxicity associated with poor survival. We found that tumor cell-specific loss of glutaminase (GLS), a key enzyme for glutamine metabolism, improved anti-tumor T cell activation in both a spontaneous mouse TNBC model and orthotopic grafts. The glutamine transporter inhibitor V-9302 selectively blocked glutamine uptake by TNBC cells but not CD8$^+$ T cells, driving synthesis of GSH, a major cellular antioxidant, to improve CD8$^+$ T cell effector function. We propose a "glutamine steal" scenario, in which cancer cells deprive tumor-infiltrating lymphocytes of needed glutamine, thus impairing anti-tumor immune responses. Therefore, tumor-selective targeting of glutamine metabolism may be a promising therapeutic strategy in TNBC.

Introduction

Rapidly dividing cells display unique metabolic traits that support their enhanced energy requirements and ever-increasing biomass (amino acids, nucleotides, lipids, etc.) synthesis to enable continued proliferation (1–9). The ability of cancer cells to hijack these metabolic processes is a known hallmark of cancer (10). While glucose metabolism received substantial attention, the role of amino acid metabolism in tumorigenesis and tumor progression has started to be explored more recently (11–14). Some cancer types are particularly dependent on metabolism of the amino acid glutamine for tumor cell survival and/or proliferation. For example, triple-negative breast cancers (TNBC), which do not express estrogen receptor (ER), progesterone receptor (PR), or human epidermal growth factor (EGF) receptor 2 (HER2), are particularly "addicted" to glutamine as compared to other breast cancer subtypes (15, 16). TNBCs often express high levels of ASCT2, a glutamine transporter, and glutaminase (GLS), the enzyme that catalyzes the rate limiting step in glutaminolysis, the conversion of glutamine into glutamate (17–19). Unlike other breast cancer subtypes, TNBCs do not have the benefit of molecularly-targeted therapies, relying primarily on chemotherapeutic regimens. However, a growing body of evidence demonstrates that glutamine is required for TNBC tumor cell survival (17–20), suggesting that glutamine metabolism may represent a therapeutic target in TNBC.

Like tumor cells, activation of T lymphocytes increases glutamine uptake and metabolism to support mitochondrial anaplerosis, nucleotide synthesis, amino acid

production, and redox balance (21). Ligation of CD3 and CD28 on T cells, events that drive T cell expansion and activation, leads to upregulation of the glutamine transporters such as ASCT2, SNAT1, and SNAT2 to facilitate glutamine uptake by T cells (22–24). Further, glutamine starvation of T cells significantly hinders T cell proliferation and cytokine production (22), illustrating the critical nature of glutamine metabolism for T cell mediated immune responses. Although ASCT2 loss from T cells did not appear to limit T cell proliferation or cytotoxicity in the acute setting of viral infection in vivo (25), chronic GLS inhibition blocked conversion of glutamine to glutamate and reduced long-term CAR-T cell responses in an in vivo tumor model (26). Of note, immunosuppressive T regulatory cells (Tregs) are able to maintain reserve respiratory capacity and thrive even in the absence of glutamine (27). Together, these studies suggest that glutamine supply to and metabolism in T cells influence the nature and potency of immune responses, but also suggest that glutamine transporter blockade may not fully impede glutamine uptake into T cells.

The increased metabolic demands of tumor cells and activated T lymphocytes may introduce competition for glutamine within the tumor microenvironment (8, 28–30), creating a scenario in which tumor cells out-compete T cells for local glutamine and thereby alter the characteristics of the TILs. Thus, in this scenario the nutrient consumption would both promote proliferation and survival of tumor cells and simultaneously limit the capacity for T cell-mediated anti-tumor immunity, similar to observations with glucose (31, 32). Accordingly, we hypothesized that glutamine-

4

dependent tumors, such as TNBCs, might benefit therapeutically from inhibition of glutamine metabolism, improving anti-tumor T cell responses by reversing a tumor "glutamine steal" phenomenon.

In this report, we analyzed human clinical basal-like breast cancer (BLBC) datasets and found an inverse relationship between glutamine metabolism and T cell cytotoxicity markers and a poor overall survival in patients whose tumors harbor both high glutamine metabolism and low T cell cytotoxicity signatures. Using spontaneous genetically-engineered and orthotopically grafted mouse models of TNBC, we show that tumor cell-specific GLS loss increased tumor interstitial glutamine concentration and intratumoral T cell infiltration and activity. Pharmacological inhibition of glutamine uptake using the glutamine transporter inhibitor, V-9302, blocked glutamine uptake in tumor cells but not in T cells, which adapted through compensatory upregulation of another glutamine transporter, resulting in superior T cell responses within tumors while diminishing tumor growth. Together, these data indicate that tumor-selective blockade of glutamine uptake may be a feasible, molecularly-targeted approach to combat TNBC, providing a two-pronged attack that boosts anti-tumor immune responses while concurrently crippling tumor cell metabolism.

Results

Expression of glutamine metabolism genes inversely correlate with cytotoxic gene signatures in human basal-like breast cancer.

To examine if tumor cell glutamine metabolism may negatively affect anti-tumor immunity in TNBC, we analyzed BLBC expression datasets curated by The Cancer Genome Atlas (TCGA). BLBCs are the molecularly defined breast cancer subtype characterizing most TNBC specimens (33). Gene expression values for genes encoding glutamine-utilizing enzymes (*GLS*, *ASNS*, and *GFPT1*) as well as glutamine transporters (ASCT2/*SLC1A5*, SNAT1/*SLC38A1*, SNAT2/*SLC38A2*, and ATB$^{0,+}$/*SLC6A14*) were used to generate a glutamine metabolism gene signature (Figure 1A). To avoid a potentially confounding bias from more highly glycolytic tumor samples, a glycolysis signature consisting of expression values for the genes encoding glycolysis enzymes was used to identify those tumor samples with reduced glycolysis (Figure 1A). The resulting "glutamine metabolism high" subset of patient samples exhibit a significantly stronger expression profile for glutamine metabolism than glycolysis, while all others are classified as having "mixed metabolism". A CTL gene signature was generated using four genes often associated with increased CD8$^+$ T cell cytotoxic activity, *GZMA*, *GZMB*, *PRF1*, and *IFNG*. Correlation analyses of the glutamine metabolism high samples revealed a strong negative correlation between the glutamine metabolism and CTL gene signatures (Figure 1B, black). The same relationship between the two parameters was not observed in the mixed metabolism samples (Figure 1B, pink). Similarly, inverse correlations were observed between *GLS*,

the rate-liminting enzyme in glutaminolysis, and the CTL gene signature (Figure 1C). Comparable trends between glutamine metabolism markers and individual markers of CTL expansion and effector function (*GZMA, GZMB, PRF1,* or *IFNG*) alone (Supplemental Figure 1A) were also oberved, suggesting that a strong antithetical relationship exists between glutamine metabolism and cytotoxic factors in basal-like breast tumors.

To evaluate whether glutamine metabolism and CTL activity may influence TNBC patient survival, we stratified BLBC patients based on their tumor glutamine metabolism (GMGS) as well as their CTL gene signatures (Figure 1D). Patients were then classified into four categories: GMGS^{LOW}/CTL^{HIGH}, GMGS^{LOW}/CTL^{LOW}, GMGS^{HIGH}/CTL^{HIGH}, or GMGS^{HIGH}/CTL^{LOW}, and a Kaplan-Meier plot was used to display patient survival for each group (Figure 1D). Having high expression of glutamine metabolic genes combined with low CTL expression resulted in reduced overall survival as well as distant metastasis-free survival compared to other groups (Figure 1D, Supplemental Figure 1B). Furthermore, survival was significantly reduced when only assessing CTL gene expression with *GLS* alone (Supplemental Figure 1C). Together, these data suggest that high glutamine metabolism along with low cytotoxic potential of T cells within tumors may contribute to poorer outcomes in TNBC patients.

Loss of glutaminase in tumor cells reduces E0771 tumor growth and metastasis in a lymphocyte-dependent manner.

7

Given that human TNBC cells have increased GLS and glutaminolysis and that T cells require glutamine metabolism for proper activation and function (17–19), we assessed the impact of cancer cell-specific glutamine metabolism on T lymphocytes within the tumor microenvironment using a mouse TNBC model. We used CRISPR-Cas9 technology in the murine TNBC line E0771 (33, 34) to generate clonal variants with glutaminase (GLS) loss-of-function mutations (Supplemental Figure 2A), referred to here as E0771-GLS^{KO}. Intracellular glutamate, a measure of glutaminolysis, was significantly decreased in the E0771-GLS^{KO} clones (Supplemental Figure 2B), confirming decreased glutaminolysis in the E0771-GLS^{KO} cells. Next, wild-type (WT) or GLS^{KO} cells were orthotopically implanted into the inguinal mammary fat pads of female C57BL/6 mice. Tumors were detected in 100% of mice from each group; however, tumor growth was diminished substantially in E0771-GLS^{KO} tumors, as measured by tumor volume (Figure 2A) and tumor weight (Figure 2B). Immunohistochemical (IHC) analysis of tumors identified abundant GLS expression in E0771-WT tumors but not in E0771-GLS^{KO} tumors (Figure 2C). Ki67 was used as a measure of tumor cell proliferation, and despite the smaller size of E0771-GLS^{KO} tumors, Ki67 was detected at similar proportions in E0771-GLS^{KO} and E0771-WT tumors (Figure 2D), suggesting that changes in tumor cell proliferation do not account for diminished tumor growth in the absence of GLS. Further, these data suggest that while E0771 murine TNBC tumor cells import and convert glutamine to glutamate, these tumors are not specifically dependent upon glutamine metabolism for their growth in vivo, making these tumors an ideal model for assessing the impact of tumor glutamine metabolism on cells of the tumor

microenvironment.

To evaluate the role of tumor-associated lymphocytes in the observed reduction of E0771-GLS^{KO} tumor growth and metastasis, E0771-WT and E0771-GLS^{KO} cells were inoculated into the mammary fat pads of Rag1 WT (*Rag1$^{+/+}$*) or Rag1-deficient (*Rag1$^{-/-}$*) mice, which lack mature B and T lymphocytes (35). In *Rag1$^{+/+}$* mice, E0771-GLS^{KO} tumors grew more slowly than E0771-WT (Figure 2E-F). However, E0771-GLS^{KO} tumors grew at a similar rate to E0771-WT tumors when grown in the lymphocyte-devoid microenvironment of *Rag1$^{-/-}$* mice. Further, IHC for the apoptosis marker cleaved caspase-3 was elevated in E0771-GLS^{KO} tumors grown in lymphocyte replete *Rag1$^{+/+}$* mice, but not in lymphocyte-devoid *Rag1$^{-/-}$* mice (Figure 2G). Similarly, fewer metastatic lung lesions were observed in E0771-GLS^{KO} tumor-bearing *Rag1$^{+/+}$* mice, but this difference was lost in *Rag1$^{-/-}$* animals (Figure 2H-I). Together, these data suggest that lymphocytes are necessary to induce tumor cell death and reduce tumor metastasis in E0771-GLS^{KO} tumors.

Loss of glutaminase in mammary epithelia reduces tumor latency and growth, while significantly enhancing T cell activation in the *C3(1)-TAg* transgenic mouse model.

To assess the role of TNBC cell glutamine metabolism on multi-step tumorigenesis, we used a genetically-engineered spontaneous model, *C3(1)-TAg*, which expresses the SV40 large T antigen (TAg) in mammary epithelial cells (MECs) of female mice via the

promoter for the C3(1) component of the rat prostate steroid binding protein (PSBP) (36). Importantly, genetic profiling studies showed that the *C3(1)-TAg* mouse model recapitulated BLBC gene signatures seen in human TNBC/BLBC specimens, including an abundance of genes representing proliferation, cell cycle pathways, and chromosome instability gene-signatures (37, 38). *C3(1)-TAg* mice were crossed into genetically engineered mice with floxed *GLS* alleles (*GLS$^{FL/FL}$*) (26) and with transgenic *MMTV-Cre* mice expressing Cre recombinase (39), allowing for Cre-mediated recombination at floxed *GLS* alleles in mammary epithelial cells (39). While *C3(1)-TAg; GLS$^{FL/FL}$* mice lacking *MMTV-Cre* (referred to here as *TAg-GLS$^{FL/FL}$*) developed tumors with an average latency of 34.4 weeks, latency was significantly delayed to 40.2 weeks in *C3(1)-TAg; MMTV-Cre; GLS$^{FL/FL}$* (referred to as *TAg-GLS$^{\Delta/\Delta}$*) (Figure 3A). Kaplan-Meier analysis of survival in tumor-bearing mice revealed extended survival in *TAg-GLS$^{\Delta/\Delta}$* mice as compared to *TAg-GLS$^{FL/FL}$* (Figure 3B). To rule out the potentially skewing effects of delayed tumor latency on apparent tumor volume measurements as a function of mouse age, we instead set the time of initial tumor palpation as T=0, then assessed tumor volumes in the weeks following initial tumor palpation. This approach revealed markedly reduced growth of *TAg-GLS$^{\Delta/\Delta}$* tumors as compared to *TAg-GLS$^{FL/FL}$* (Figure 3C). Histological analysis of tumors collected from mice at humane endpoints revealed dense, highly cellular tumors with tightly packed nuclei in *TAg-GLS$^{FL/FL}$* mice. However, vast central areas lacking tumor cellularity were noted in *TAg-GLS$^{\Delta/\Delta}$* tumors (Figure 3D). IHC detection of GLS confirmed loss of GLS protein expression in *TAg-GLS$^{\Delta/\Delta}$* tumors (Figure 3E).

In order to assess how tumor cell-specific glutaminase impacts T cells within the tumor microenvironment, T cell populations were analyzed from tumor single cell suspension using flow cytometry (Supplemental Figure 3A). Because tumor size may affect anti-tumor immunity, we analyzed tumors harvested at 2 weeks after initial tumor palpation, a time point when both groups dispayed similar tumor volumes and weights (Figure 3F). *TAg-GLS*$^{\Delta/\Delta}$ tumors harbored significantly increased levels of CD45$^+$ immune cells and CD45$^+$CD3$^+$ tumor infiltrating lymphocytes (TILs) (Supplemental Figure 3B-C), with greater enrichment of CD3$^+$CD8$^+$ T cells (Figure 3G, Supplemental Figure 3D). Cytotoxic CD8$^+$ T cells directly carry out their killing activity via release of the serine protease, granzyme B (GZMB) (40), and consistent with increased effector function, *TAg-GLS*$^{\Delta/\Delta}$ tumors harbored increased granzyme B (GZMB)$^+$ CD8$^+$ T cells compared to *TAg-GLS$^{FL/FL}$* controls (Figure 3H, Supplemental Figure 3E). *TAg-GLS*$^{\Delta/\Delta}$ tumors also displayed increased cytotoxic T lymphocytes (CTL) expressing the degranulation marker CD107a (Figure 3I, Supplemental Figure 3F), the pro-inflammatory cytokine interferon-γ (IFNγ) (Figure 3J, Supplemental Figure 3G), as well as the cell activation markers CD25 and CD44 (Supplemental Figure 3H-J). Tumor cell loss of GLS also resulted in a modest increase in both the number of IFNγ-producing CD4$^+$ Th1 T helper cells and the IFNγ MFI (Figure 3K, Supplemental Figure 3K). Smaller increases were observed in the IL-4$^+$ Th2 as well as the FoxP3$^+$ and FoxP3$^+$CD25$^+$ Treg CD4$^+$ T cell populations in *TAg-GLS*$^{\Delta/\Delta}$ tumors, whereas a small decrease in the IL-17A$^+$ Th17 population was detected although these changes were not associated with increased cytokine production or FoxP3 expression (Figure 3L-N, Supplemental Figure 3L-Q).

Interestingly, the proportion of CD4$^+$ T-cells expressing activation markers CD25, CD69, and CD44 was largely unchanged, suggesting that cumulative CD4$^+$ T cell activation may not be occurring in *TAg-GLS*$^{-/-}$ tumors (Supplemental Figure 3R-T). Together, these findings suggest that targeting tumor-specific glutaminase improves CD8$^+$ T cell activation and effector capacity with this TNBC model.

Tumor cell GLS deficiency in established tumors increases T cell numbers and effector function

T cell numbers and activation markers were also examined in orthotopic E0771-WT and E0771-GLS^{KO} tumors grown in WT C57BL/6 mice. Flow cytometric tumor anlayses identified increased numbers of CD45$^+$ tumor-associated leukocytes and CD45$^+$CD3$^+$ T-cells in E0771- GLS^{KO} tumors as compared to E0771-WT (Supplemental Figures 4A-B). The percentage of the CD45$^+$ population that was also CD3$^+$CD8$^+$ was increased in E0771-GLS^{KO} tumors compared to the WT controls (Figure 4A). A trend towards an increased percentage of CD45$^+$ tumor leukocytes that were CD4$^+$ was also seen in E0771-GLS^{KO} tumors. When normalized to total tumor mass, the numbers of both CD4$^+$ and CD8$^+$ T cells were increased in E0771-GLS^{KO} tumors as compared to controls (Figure 4B).

Further, CD8$^+$ T cells expressing mature CTL effector markers were increased in E0771-GLS^{KO} tumors, including those expressing GZMB (Figure 4C), CD107a (Figure 4D), and interferon-γ (Figure 4E), while CTL activation markers were also increased,

including CD25, CD69 and CD44, (Supplemental Figures 4C-E), suggesting that GLS

loss from the tumor epithelia may indirectly enhance the differentiation and effector

activity of CD8$^+$ T cells. E0771-GLS^{KO} tumors also exhibited an increased presence of

CD4$^+$IFNγ$^+$ Th1 cells (Figure 4F), although the number of the CD4$^+$IL-4$^+$ Th2 cells was

not significantly altered by GLS loss from tumor cells (Figure 4G). Interestingly, CD4$^+$IL-

17A$^+$ Th17 populations were also increased in E0771-GLS^{KO} tumors (Figure 4H,

Supplemental Figure 4F), although no significant changes were observed in Tregs

(Figure 4I, Supplemental Figure 4F). Additionally, the number of CD4$^+$ T cells from

E0771-GLS^{KO} tumors expressing activation markers CD25, CD69, and CD44 was

increased, consistent with increased CD4$^+$ T cell activation (Supplemental Figure 4G-I).

Collectively, these data suggest that deletion of GLS in TNBC tumor cells enhances the

number and effector function of tumor infiltrating T cells, possibly through changes in the

metabolite availability within the tumor microenvironment in which these lymphocytes

must function.

**Loss of GLS in tumor cells increases interstitial glutamine and enhances antigen-
specific anti-tumor CD8$^+$ T cell infiltration**

Glutamine is an abundant amino acid in the blood stream, but glutamine supply can

vary in the tissue interstitum (41, 42). Notably, glutamine concentrations measured

within tumor interstitial fluid collected from E0771-WT tumors was approximately 100

µM, whereas E0771-GLS^{KO} interstitial tumor glutamine levels were nearly 700 µM

(Figure 4J), similar to the reported plasma glutamine concentration of C57BL/6 mice

(41, 43). These data suggest that GLS loss from tumor cells prevents tumor cell-driven

glutamine depletion within the interstitium, which may provide more available glutamine

for other cells in the tumor microenvironment, including lymphocytes. Indeed, we

observe that IFNγ secretion from effector type I CD8$^+$ T cells (Tc1) was significantly

increased in response to elevated glutamine (Figure 4K), suggesting that greater

glutamine availability in GLS^{KO} tumor interstitium may directly improve cytotoxic T cell

effector responses.

To analyze how tumor cell glutamine metabolism may regulate an antigen-specific T cell

response, we utilized E0771(OVA)-WT and E0771(OVA)-GLS^{KO} cells expressing the

full-length ovalbumin (OVA) protein (Supplemental Figure 4J-K). Ovalbumin peptides

are processed for presentation of the OVA$_{257-264}$ antigenic peptide (SIINFEKL) on MHC

Class I (H2K^b) molecules (44). CD8$^+$ T cells expressing a SIINFEKL-specific T cell

receptor (TCR) (45, 46) were purified from OT-I transgenic mice (Supplemental Figure

4L), transduced ex vivo to overexpress GFP, and then primed with SIINFEKL peptide.

Following E0771(OVA) tumor engraftment, adoptive transfer of OT-I GFP$^+$CD8$^+$ T cells

into tumor-bearing mice enabled immunofluorescent visualization of CTL tumor

infiltration (Figure 4L). Although OT-I GFP$^+$CD8$^+$ T cells were detected in all tumors,

GFP$^+$ cells were more abundant in E0771(OVA)-GLS^{KO} tumors (Figure 4M). Flow

cytometry confirmed this observation, revealing nearly twice as many GFP$^+$CD8$^+$ T cells

from E0771-GLS^{KO} tumors as compared to E0771-WT tumors (Figure 4N). Together,

these results suggest that inhibition of glutamine utilization within tumor cells increases

the intratumoral CD8$^+$ T cells.

Glutamine transporter inhibition by V-9302 reduces tumor growth and improves T cell activation

Since genetic models of impaired tumor cell glutaminolysis resulted in decreased tumor growth, increased glutamine concentrations in the tumor interstitium, and improved TIL numbers, we tested the hypothesis that pharmacologic blockade of glutamine metabolism might significantly diminish growth and support T-cell activity in TNBC models. Early clinical studies of the GLS inhibitor CB-839 demonstrated tolerability and safety, but with limited efficacy as a single agent in TNBC (47). However, V-9302, a small molecule amino acid transporter inhibitor with a greater selectivity for reducing glutamine uptake (48, 49), was more efficacious for inducing TNBC cell death in cell culture models, including the human TNBC lines MDA-MB-231 and HCC1806 and the mouse TNBC lines 4T1 and E0771 (Supplemental Figure 5A-D). Furthermore, V-9302 reportedly has little to no negative impact on CD44 expression on CD8$^+$ T cells ex vivo (48). To test the impact of glutamine uptake inhibition with V-9302, orthotopic E0771 tumors grown in immune competent C57BL/6 female mice were treated daily with V-9302 (50mg/kg) or vehicle beginning when tumors reached 100 mm^3, equivalent to 11 days after tumor cell inoculation. Tumors treated with V-9302 treatment displayed markedly reduced tumor growth (Figure 5A), resulting in decreased tumor weight upon collection at day 16, after only 5 days of treatment (Figure 5B). While V-9302 had only a marginal impact on Ki67$^+$ proliferation, there was a more significant (3-fold) increase

in apoptosis, as measured by cleaved caspase-3 (Figure 5C), in agreement with the increased cell death seen upon genetic GLS loss in E0771 tumors.

Interestingly, the number of CD45$^+$ leukocytes was not significantly impacted by 5 days of V-9302 treatment (Supplemental Figure 5E), nor were the total number of CD45$^+$CD3$^+$ T cells (Supplemental Figure 5F). While total CD8$^+$ T cell frequencies were unaffected by V-9302 treatment (Figure 5D), detailed histological assessment identified CD8$^+$ T cells as being restricted to the periphery of vehicle-treated E0771 tumors, while an increased CD8$^+$ T cell infiltration deeper into the tumor core (>500 μm) was seen in tumors treated with V9302 (Figure 5E). Changes in localization from the periphery to the intra-tumoral core have been described previously, correlating with immune response to therapeutic immune checkpoint inhibition in several tumor models (50–52). We next assessed how V-9302 impacted CD8$^+$ TIL activation and effector markers. Tumors treated with V-9302 harbored CD8$^+$ T cell populations producing granzyme B (Figure 5F), CD107a (Figure 5G), IFNγ (Figure 5H), CD25, CD69, and CD44 (Supplemental Figure 5G-H), confirming CTL effector capacity and activation in response to V-9302. Additionally, CD4$^+$ TILs from tumors treated with V-9302 displayed an increased population of IFNγ producing cells, suggesting an increased CD4$^+$ Th1 T cell phenotype upon V-9302 treatment (Figure 5I). Only smaller increases in the Th2 (IL-4) and Th17 (IL-17A) populations were observed (Figure 5J, Supplemental Figure 5I). In contrast, the CD4$^+$Treg$^+$CD25$^+$CD127^{lo} Treg population was significantly decreased in V-9302-treated tumors, although the FoxP3$^+$ populafion was not changed (Figure 5K,

Supplemental Figure 5J). The frequency of CD4$^+$ T cell populations expressing the

activation markers CD25, CD69, and CD44 were also increased (Supplemental Figure

5K-L). Together, these data confirm that V-9302 increases tumor cell death while

simultaneously augmenting CD8$^+$ CTLs and CD4$^+$ Th1 phenotypes within the TNBC

tumor microenvironment.

Compared to effector memory or terminally differentiated effector T cells, CD8$^+$ central

memory T cells support a more persistent anti-tumor response (53, 54). To assess

whether V-9302 may support long-term cytotoxicity, we evaluated the CD44$^+$CD62L$^+$

central memory (T_{CM}) and CD44$^+$CD62L$^-$ effector memory (T_{EM}) T cell populations.

Treatment of ex vivo activated splenocytes with V-9302 significantly increased the

T_{CM}:T_{EM} ratio of CD8$^+$ T cells but not CD4$^+$ T cells (Supplemental Figure 5M-N).

However, both the central memory and effector memory populations were increased in

V-9302-treated tumors (Supplemental Figure 5O-P), suggesting that V-9302 improves

anti-tumor responses in part through supporting persistant memory T cells.

The glutamine transporter inhibitor V-9302 increases glutamine uptake and

glutathione synthesis in cytotoxic T cells.

To investigate the underlying molecular mechanisms regulating increased T cell

activation upon treatment with V-9302, splenocytes harvested from wild-type mice and

cultured ex vivo were primed with anti-CD3 and anti-CD28 antibodies in the presence or

absence of V-9302 (10µM for 48 hrs). As expected, CD3/CD28 priming increased the

viable percentage of the total CD8$^+$ T cell population, as compared to splenocytes not primed with CD3/CD28 (Supplemental Figure 6A). Importantly, V-9302 did not affect the proportion of viable CD8$^+$ T cells following CD3/CD28 priming (Supplemental Figure 6A), nor did V9302 affect the viable CD4$^+$ T cell population (Supplemental Figure 6B). Previous studies demonstrate that CD3/CD28 priming of T cells activates the mTORC1 signaling pathway, resulting in phosphorylation of the mTORC1 effector ribosomal protein S6 (S6RP) (55, 56). As measured by phos-flow cytometry, CD3/CD28 priming of CD8$^+$ T cells increased phospho-S6RP, which was unaffected by V-9302 (Supplemental Figure 6C). Similarly, V-9302 did not significantly alter phospho-S6RP in CD4$^+$ T cells (Supplemental Figure 6D). The cytotoxic capabilities of OT-I CD8$^+$ T cells against E0771(OVA) tumor cells were assessed in co-culture studies performed in the presence and absence of V-9302. Importantly, OT-I CD8$^+$ T cells were poorly cytotoxic against parental E0771 cells, but displayed potent cytotoxicity against E0771(OVA) cells, confirming antigen-directed cytotoxicity against tumors cells (Figure 6A). Notably, treatment with V-9302 increased T cell-dependent cytotoxicity in this assay nearly 2-fold, indicating that V-9302 enhances the ability of CD8$^+$ T lymphocytes to kill tumor cells. These studies suggest that V-9302 enhances the cytotoxicity of CD8$^+$ T cells but has no significant impact on mTORC1 activation or T cell viability upon T cell receptor (TCR) stimulation, despite the well documented requirement for glutamine uptake and glutaminolysis in T cell viability and activation.

Still, similar to our observation in a GLS deletion model, V-9302 increased the tumor

interstitial glutamine concentration (Figure 6B), indicating that V-9302 may improve

glutamine availability for T cells. These observations were assessed further by

measuring ^{3}H-glutamine uptake in CD3/CD28-primed CD8$^+$ T cells co-cultured with

E0771 tumor cells. After pulsing for 15 min with ^{3}H-glutamine, tumor cells and CD8$^+$ T

cells were assessed separately for ^{3}H-glutamine uptake. While ^{3}H-glutamine was

detected in E0771 cells upon co-culture with CD8$^+$ T cells, treatment of co-cultures with

V-9302 diminished ^{3}H-glutamine uptake by E0771 tumors nearly 40% (Figure 6C). In

contrast, V-9302 treatment did not diminish ^{3}H-glutamine uptake by CD8$^+$ T cells, and

even increased CD8$^+$ T cell ^{3}H-glutamine uptake, a differential effect that was also seen

in isolated cells (Supplemental Figure 7A-B). Similar results were seen when this

experiment was repeated in HCC1806 human TNBC cells co-cultured with human

peripheral CD8$^+$ lymphocytes (Figure 6D), confirming that V-9302 affected glutamine

uptake by TNBC cells, but not by CD8$^+$ T cells. Importantly, expression of the

ASCT2/*Slc1a5*, the sodium-coupled neutral amino acid transporter family members

SNAT1/*Slc38a1* and SNAT2/*Slc38a2* , as well as the L-type amino acid transporter

LAT1/*Slc7a5* and its co-transporter 4F2HC/*Slc3a2*, were unchanged in E0771, 4T1, and

CD8$^+$ T cells in the presence of V-9302 (Supplemental Figure 7C-G). Interestingly, the

Na$^+$/Cl$^-$ dependent neutral and cationic amino acid transporter ATB$^{0,+}$/*Slc6a14* was

upregulated nearly 6-fold in CD8$^+$ T cells, but not TNBC tumor cells, treated with V-9302

(Figure 6E). Despite low ATB$^{0,+}$ protein expression in control CD8$^+$ T cells, western

analysis confirmed ATB$^{0,+}$ protein upregulation in CD8$^+$ T cells in response to V-9302

treatment to levels more comparable to those observed in TNBC cells (Figure 6F).

To assess whether $ATB^{0,+}$/*Slc6a14* may compensate for glutamine transporter inhibition by V-9302 in $CD8^+$ T cells, we evaluated ^{3}H-glutamine uptake in anti-CD3/CD28-primed $CD8^+$ T cells following $ATB^{0,+}$ knockdown (Figure 6G, Supplemental Figure 7H). Consistent with our co-culture system, V-9302 increases ^{3}H-glutamine uptake in isolated CD8+ T cells (Figure 6G). However, ^{3}H-glutamine uptake was significantly reduced following $ATB^{0,+}$ knockdown (Figure 6G). Likewise, inhibition of $ATB^{0,+}$ using 2-aminobicyclo(2.2.1)heptane-2-carboxylic acid (BCH) (57), an inhibitor of LAT1 and $ATB^{0,+}$, or α-methyltryptophan (αMT), a selective $ATB^{0,+}$ inhibitor (58), significantly reduced ^{3}H-glutamine uptake in anti-CD3/CD28-primed $CD8^+$ T cells (Figure 6H). In contrast, N-methyl-aminoisobutyric acid (MeAIB), an inhibitor of SNAT1/SNAT2 (49), had no effect on ^{3}H-glutamine uptake (Figure 6H), suggesting that $ATB^{0,+}$/*Slc6a14* may be the primary transporter involved in glutamine influx of activated $CD8^+$ T cells in the presence of V-9302. Overexpression of the the rat $ATB^{0,+}$/*Slc6a14* ortholog in pre-activated $CD8^+$ T cells resulted in increased ^{3}H-glutamine uptake at similar levels observed with V-9302 treatment (Figure 6I, Supplemental Figure 7I-J) and conferred greater antigen-specific cytotoxicity to $CD8^+$ OT-I T cells against TNBC tumor cells in vitro (Figure 6J). Together, these results suggest that compensatory upregulation of the glutamine transporter $ATB^{0,+}$/*Slc6a14* in V-9302 treated $CD8^+$ T cells sustains glutamine uptake by T cells despite partial glutamine transporter inhibition, thus maintaining glutamine-dependent T cell cytotoxicity against tumor cells in V-9302-treated tumors. However, compensatory upregulation of glutamine transport was not seen in V-9302-treated TNBC cells, perhaps explaining their exquisite sensitivity to V-9302.

As a requirement to support effector functions, activated CD8+ T cells utilize glutamine to support numerous metabolic processes, including energy production and redox maintenance (21). To assess whether V-9302 impacts T cell enegetics, we measured respiration of CD8$^+$ TILs isolated from tumors treated with vehicle or V-9302 (Supplemental Figure 7K-L). Although glutamine influx is enhanced in the presence of V-9302, the drug does not change the oxygen consumption rate (OCR) of CD8$^+$ TILs. However, ex vivo anti-CD3/CD28-primed CD8$^+$ T cells cultured in V-9302 are more dependent on glutamine to carry out respiration (Supplemental Figure 7M).

Since overall respiration was not affected, we next evaluated if V-9302 and enhanced glutamine influx improved the redox balance of CD8$^+$ T cells by first evaluating glutathione (GSH) levels. Indeed, CD3/CD28-primed CD8$^+$ T cells cultured in V-9302 had increased glutathione levels compared to the vehicle control (Figure 6K). De novo glutathione synthesis involves ligation of glutamate with the amino acid cysteine by the glutamate-cysteine ligase (GCL). Consistent with increased glutathione production, activated CD8$^+$ T cells cultured in V-9302 show increases in intracellular cysteine, but not alanine or asparagine, potentially through increased expression of the cysteine transporter, xCT (Figure 6L-M, Supplemental Figure 7N-O). Expression of GCLC, the catalytic subunit of GCL, was also increased in the CD8$^+$ and CD4$^+$ TILs isolated from mice treated with V-9302 (Figure 6N, Supplemental Figure 7P). These increases in glutathione synthetic components following V-9302 treatment are coupled with a decrease in ROS levels of both CD4$^+$ and CD8$^+$ effector T cells (Figure 6O,

Supplemental Figure 7Q). Together, these data suggest that V-9302 improves

glutamine uptake to support de novo glutathione synthesis and improved redox balance

in T cells (Figure 6P).

Discussion:

Breast cancer is the most prevalent malignancy in women, encompassing 30% of all new cancer diagnoses, and the second leading cause of cancer-related death. Advances in targeted therapies have improved the survival of ER+ and HER2+ breast cancers, but the prognosis of triple-negative/basal-like breast cancer (TNBC), the most aggressive and refractory subtype, remains grim. In search of vulnerabilities for these cancers, TNBCs were found to be dependent on glutamine metabolism (15–19). However, key questions that are critical for drug development remain unanswered, including how tumor cell-derived glutamine metabolism effects immune function and whether inhibitors of glutaminase and glutamine transporters have an impact on anti-tumor immunity. In this report, we show that tumor cell-specific glutamine metabolism suppresses tumor infiltrating T lymphocyte numbers and function, perhaps contributing to the non-responsiveness of a significant number of TNBCs to immunotherapies observed in the clinics (59). Further, we show that TNBC tumors have increased susceptibility to V-9302, a ASCT2/SNAT2 inhibitor, whereas the cytotoxic T cells upregulate alternative transporters to sustain glutamine uptake and effector function. Thus, preferential inhibition of glutamine metabolism in tumor cells may represent a promising targeted therapy that enhances anti-tumor immune responses in TNBC patients.

The tumor microenvironment (TME) is a diverse landscape, containing a variety of cell types including tumor cells, immune cell populations (lymphocytes, macrophages,

natural killer (NK) cells, dendritic cells, myeloid-derived suppressor cells (MDSCs), etc.),

fibroblasts, and endothelial cells among others (60, 61). Our data suggests that at least

two of these populations, tumor cells and T lymphocytes, consume glutamine in the

tumor interstitium. However, many of these additional populations also consume and

utilize numerous metabolites, including glutamine. For example, M1 macrophage

differentiation is favored upon glutamine synthetase (GS) inhibition due to greater

accumulation of succinate (62), while GLS activity is crucial for endothelial cell

proliferation and retinal angiogenesis in vivo (63). Therefore, the possibility remains that

targeting tumor cell glutamine metabolism may alter additional cell populations present

in the tumor microenvironment. Given that Rag1-deficiency essentially eliminated the

anti-tumor effects of GLS LOF, our results suggest that lymphocytes are the primary

anti-tumor effectors in a glutamine-improved tumor microenvironment. However, other

immune cells may also be affected by inhibition of glutamine metabolism. For example,

the production of α-ketoglutarate (αKG) via glutaminolysis is important for activation

of M2-like macrophages (64), and a prodrug of the glutamine antagonist DON was

recently shown to inhibit generation and recruitment of MDSCs (65). Thus, although our

findings of improved intratumoral T cell effector functions likely result from the increased

glutamine availability to T cells, the potential remains for additional factors that can

impact immune system such as inhibition of suppressive microenvironment by M2-like

macrophage and MDSCs.

The role of glutamine metabolism in T cells has been extensively studied in recent

years, uncovering its requirement for processes such as proliferation, activation, and differentiation (21–23, 25, 26). Glutamine uptake is massively enhanced upon TCR stimulation in T lymphocytes, and is crucial for their proliferation and cytokine production as glutamine starvation severely limits these downstream processes (22). Recent evidence suggests that pre-adaptation to glutamine deprivation in vitro enhances CD8^{+} T cell responses when adoptively transferred in vivo (26, 66, 67), although the mechanisms of which were not completely understood. Such glutamine deprivation does not reflect conditions within the native tumor microenvironment (TME), where there is a measurable levels of glutamine within the tumor interstitium. Using orthotopic and spontaneous mouse models, we show that loss of GLS in tumor cells increased interstitial glutamine concentration to near physiological plasma levels (41, 43) and improved overall activation and effector capacity of T lymphocytes, indicating that reduced glutamine in the TME is immunosuppressive. Indeed, activity of effector CD8^{+} T cells measured by IFNγ secretion is increased in the presence of elevated glutamine. Likewise, pharmacological inhibition of glutamine transport using V-9302, which suppressed glutamine uptake in tumor cells but had little impact on CD8^{+} T cells, also improved T cell activation in vivo. Altogether, our results suggest that reducing glutamine metabolism specifically within tumor cells increases glutamine availability within the TME and improves T lymphocyte redox status and activation, supporting the hypothesis of glutamine competition within TNBC tumors.

Amino acid transporters involved in glutamine shuttling have been reported to have

varying roles in T cell dynamics. In one report, loss of ASCT2 impaired both Th1 and Th17 differentiation, but enhanced Treg generation without significant effect on $CD8^+$ T cells (25). Using a different mouse line, a second report showed that ASCT2 deficiency did not affect either B cells or T cells (68), leaving open the question whether pharmacological inhibition of ASCT2 will affect lymphocyte function. While SNAT1/SLC38A1 and SNAT2/SLC38A2 expression is increased after TCR-mediated activation (22, 24, 69), little is know regarding their roles in T cell development and function. Despite incomplete understanding of the mechanisms underlying phenotypes in the ASCT2/*Slc1a5*-deficient mouse models, the facts remain that (*i*) the glutamine transport inhibitor V-9302 was previously reported to have no impact on CD44 expression on $CD8^+$ T cells in vitro (48), and (*ii*) our in vivo data showed that administration of V-9302 in tumor-bearing mice increased $CD8^+$ T cell activation and increased glutathione synthesis through upregulation of $ATB^{0,+}$. A recent study showed that the glutamine antagonist DON also exhibits differential effects on tumor cells and T cells, but has broad impacts on a variety of metabolic pathways, including glutaminolysis and glycolysis (70), making it difficult to pinpoint the role of glutamine metabolism on these cell populations in vivo. Thus, the drug V-9302 or its analogs may represent an alternative approach to preferentially target tumor cells while sparing anti-tumor T cells.

Pharmacological-targeted therapies are capable of impacting multiple cell populations found within the tumor microenvironment as well as the human body. Due to the

26

glutamine-addicted nature of TNBC cells, a great deal of attention has recently been focused on targeting glutamine metabolism as a means to therapeutically target these aggressive tumors. For example, the glutaminase (GLS) inhibitor CB-839 is undergoing clinical trial testing for numerous solid tumors. While CB-839 as a single-agent therapy has not produced promising results, the pleiotropic roles of glutamine suggest that CB-839 may be a good candidate for combination therapy to induce synthetic lethal effects on cancer cells. However, it may be that throttling the supply of glutamine would be needed in some settings. Our findings that V-9302 inhibiting glutamine transport into tumor cells while enhancing Th1 and $CD8^+$ T cell activation represents a potential therapeutic strategy to preferentially target glutamine metabolism in tumor cells. Our work suggests strategies that preferentially targeting glutamine metabolism in glutamine "addicted" tumor cells may represent a more advantageous therapeutic approach to treating triple-negative breast cancer.

Methods:

Flow cytometry. Immune cell populations were identified via flow cytometry from respective dissociated whole tumor cell suspensions or cultured cells. To assess mTORC1 signaling and ROS, C57BL/6 mouse splenocytes were activated with anti-mouse CD3e (Tonbo #70-0031, 1.25 µg/mL) and anti-moue CD28 (Tonbo #70-0281, 1.25 µg/mL) while treated with vehicle (DMSO) or V-9302 (10 µM) for 48 hours. For phos-flow cytometry, cells were collected in the presence of phosphatase inhibitor and stained with 7-AAD (10 µg/mL). Fixed cells were permeabilized in cold methanol, and phospho-S6RP (pS6RP) (Ser235/236; CST #2211) was indirectly detected (Alexa Fluor 647 goat anti-rabbit secondary, 1:200, Invitrogen #A21244). T cells were identified by extracellular staining of mouse CD45, CD3e/TCRβ, CD4, and CD8a (Supplemental Figure 3A, Supplemental Table 3). To detect ROS, cells were incubated with 5 µM H_2-DCFDA (Invitrogen #D399) at 37°C for 30 min. Dead cells were excluded using Violet 510 Ghost.

For tumor immune analyses, tumors were harvested, weighed, and dissociated in RPMI-1640, 5% FBS, collagenase IA (1 mg/mL; Sigma-Aldrich #C9891), and DNase I (0.25 mg/mL; Sigma-Aldrich #DN25) for 30 min at 37°C. To obtain single-cell suspensions, digested tissue was filtered through a 70 µm cell strainer and red blood cells were lysed using ACK lysis buffer. For detection of interferon-γ (IFNγ), $1-2 \times 10^6$ cells were stimulated in RPMI-1640 containing 5% FBS, phorbol 12-myristate 13-acetate (PMA) (50 ng/mL; Sigma-Aldrich #P8139), ionomycin (1 µg/mL; Sigma-Aldrich

#I0634), and GolgiPlug protein transport inhibitor (1:1000; BD #555029) for 4 hours at 37°C. Dead cells were excluded from analysis by staining with Ghost dye Violet 450 (Tonbo #13-0863) or Violet 510 (Tonbo #13-0870), as indicated. Following blocking with αCD16/32 (mouse Fc block), extracellular staining was achieved against the following proteins: CD45, CD45.2, CD3e, TCRβ, CD4, CD8a, CD25, CD69, CD44, CD62L, CD127, and/or CD107a (Supplemental Table 3). Intracellular staining for GZMB, IFNγ, IL-4, IL-17A, and GCLC was accomplished using Cytofix/cytoperm solution kit (BD #554714) on paraformaldehyde-fixed cells, per manufacturer's directions. GCLC was indirectly detected by Alexa Fluor 647 goat anti-rabbit secondary as described above. To detect FoxP3, fixed cells were stained using the FoxP3/Transcription Factor Staining Kit (Tonbo #TNB-0607), as directed. Isolated splenocytes or tumor cell suspensions were used for unstained, compensation, fluorescence minus one (FMO), and isotype controls, where appropriate. Flow cytometry data was obtained on a BD Fortessa using BD FACS Diva software and analyzed using FlowJo software.

To assess T cell infiltration, E0771(OVA) sgLacZ (WT) or sgGls3 (GLS^{KO}) (5x10^5 cells) were bilaterally implanted into the #4 mammary fat pads of 6- to 8-week-old C57BL/6 female mice. OT-I splenocytes were isolated from 4-week-old female OT-I mice and activated with SIINFEKL peptide (1 ug/mL; Invivogen) for 72 hours. Following activation, CD8$^+$ OT-I T cells were isolated using mouse CD8a microbeads (Miltenyi #130-045-201) as described by the manufacturer and then transduced with MiG

retrovirus to overexpress GFP. GFP$^+$CD8$^+$ OT-I T cells (3x10^6) were adoptively

transferred via retro-orbital injection into tumor-bearing mice 8 days following tumor

implantation. After 3 days, tumors were harvested, processed, and analyzed by flow

cytometry as described above. Dead cells were excluded from analysis by staining with

Ghost dye Violet 510. CD8$^+$ OT-I cells were detected by GFP.

Tumor Interstitial Fluid Metabolic Assays. Tumor interstitial fluid was collected from

tumors as previously described (71), with some changes. Briefly, tumors were

harvested, weighed, and then washed with 1xPBS to remove excess blood from the

tumor surface. Excess PBS was removed by carefully blotting with a Kimwipe. Tumors

were placed in a 20 µm pluriStrainer mounted in a microcentrifuge tube, then

centrifuged at 100xg at 4°C for 30 min. The cleared interstitium was deproteinated and

glutamine was detected using the Glutamine Detection Assay Kit (Abcam, #ab197011)

according to manufacturer's instructions. Known glutamine standards were used to

calculate concentrations.

Intracellular Amino Acid Assays. To assess intracellular cysteine, alanine, and

asparagine levels, αCD3/CD28-activated CD8$^+$ T cells freshly isolated from C57BL/6

mice were cultured in vehicle or V-9302, as described above. Equal cells were

homogenized and analyzed for cysteine (Abcam #ab211099), alanine (Sigma

#MAK001), or asparagine (BioVision #K736) as described by the manufacturers.

Tumor cell intracellular glutamate concentrations were determined using the Glutamate

Assay Kit (Sigma-Aldrich #MAK004-1KT) as previously described (6) with some changes. Briefly, control or GLS loss-of-function E0771 single cell clones were cultured in glutamine-free, serum-free DMEM for 24 hours. Cells were then stimulated with L-glutamine (2.5 mM) for 15 min. Fluorescence or absorbance were measured using the BioTek Synergy HT plate reader. Amino acid concentrations were determined using known standards and reported as fold change using the appropriate control.

IFNγ Cytokine Secretion by Tc1 cells in Response to Glutamine. CD8^{+} T cells were purified from spleens of C57BL/6 mice and activated with plate-bound anti-CD3 (2.5 μg/mL) and soluble anti-CD28 (2.5 μg/mL) in the presence of irradiated APCs. CD8^{+} T cells were cultured at 1×10^6 cells per mL in 2mL on 12-well plate with 2×10^6 irradiated APCs and fed rh-IL2 (20ng/mL) every other day. Cells were split on day 2 into 6-well plates and carried for a total of 4 days. On day 4 cultures were harvested, counted and equal numbers of cells were re-plated at a density of 2×10^6 cells/mL in media with indicated concentrations of glutamine, reactivated with fresh anti-CD3 and anti-CD28 (1.25 μg/mL each), and cultured overnight in a 37°C CO_2 incubator. Culture supernatants were collected after 18-24 hours of culture for anti-IFNγ cytokine sandwich ELISA, as previously described (72), using anti-mouse IFNγ (BD #551216) and anti-mouse IFNγ-biotin (BD #554410) as capture and detection antibodies, respectively.

Cytotoxicity Assay. For in vitro cytotoxicity assays, E0771(OVA) or E0771 (1×10^4 per well) were plated in triplicate as indicated and allowed to attach for 6 hours. Tumor cells

were co-cultured with SIINFEKL-activated WT or MiG-ATB[0,+] transduced CD8^{+} OT-I

cells (2×10^3 per well, resulting in 5:1 tumor cell to CD8^{+} cell ratio) in T cell media in the

absence or presence of V-9302 (10 µg/mL), as indicated, for 48 hours. Cytotoxicity was

measured using the LDH Cell-mediated Cytotoxicity Assay (Thermo Scientific),

according to manufacturer's directions. Percent cytotoxicity was calculated following

correction for spontaneous LDH release from tumor cells and CD8^{+} T cells alone and

based on maximal LDH release for each condition.

Glutamine Uptake Assay. C57BL/6 or OT-I mouse CD8^{+} cells were isolated,

activated, and modified, as indicated. Human PMBCs were activated with functional

grade anti-human CD3 (1 µg/mL; Invitrogen #16-0038) and anti-human CD28 (1 µg/mL;

Invitrogen #16-0289), with supplementation of human IL-2 (20 U/mL) for 48 hours and

extracted using human CD8 microbeads (Miltenyi #130-045-201) as directed. E0771

(3.5×10^4 per well) or HCC1806 (1.0×10^4 per well) cells were plated in at least duplicate

in a 96-well plate, and cells were allowed to attach overnight, as indicated. Glutamine

uptake was measured in tumor or CD8^{+} cells in isolation or tumor/CD8^{+} cell co-cultures

(1:1) as described previously (48), with a few alterations including omission of BCH

except where specified. Briefly, tumor cells and/or CD8^{+} cells were washed three times

in uptake buffer (10 mM HEPES pH 7.4, 137 mM NaCl, 5.1 mM KCl, 0.77 mM KH_2PO_4,

0.71 mM $MgSO_4$, 1.1 $CaCl_2$, and 10 mM D-glucose). CD8^{+} T cells were resuspended in

assay buffer containing V-9302 (10 µM), N-methyl-aminoisobutyric acid (MeAIB, 10mM)

(Sigma #M2383), 2-aminobicyclo(2.2.1)heptane-2-carboxylic acid (BCH, 500 µM)

(Cayman Chemical #15249), and/or α-methyl-DL-tryptophan (αMT, 100 μM) (Sigma

#M8377), as indicated, along with the appropriate vehicles. For co-culture assays,

CD8$^+$ cells were directly added to tumor cells. Following a 15 min incubation at 37°C, 1

μCi of L-[2,3,4-3H]-Glutamine (American Radiolabeled Chemicals #ART-0149) was

added, and cells were incubated an additional 15 min. Suspended CD8$^+$ cells were

removed, and both tumor and T cells were washed in uptake buffer separately. Cells

were lysed with 1 N NaOH, and radioactivity was measured using a Beckman LS 6500

Scintillation counter for 1 min and recorded as counts per minute (CPM). Treated

samples were normalized to the appropriate controls.

Glutathione Assay. CD8+ T cells were activated and cultured in the presence of

vehicle or V-9302, as described above. Glutathione was measured using the GSH-Glo

Glutathione Assay (Promega #V6911) according to manufacturer's instructions.

Luminescence was measured using the BioTek Synergy HT plate reader. Glutathione

concentrations were determined from a known standard.

Quantitative Real-Time Polymerase Chain Reaction. E0771 or 4T1 cells (5x10^5)

were plated and treated with vehicle or 10 μM V-9302 for 48 hours. Likewise, isolated

activated primary mouse splenocytes were treated with vehicle or V-9302, followed by

isolation of CD8$^+$ cells as described above. RNA was collected using the RNeasy kit

(Qiagen), and cDNA was generated using the iScript cDNA synthesis kit (Bio-Rad)

according to manufacturers' directions. Samples were amplified in triplicate using

SYBR Green PCR Master Mix (Thermo Fisher), 10 pmol of primer (Supplemental Table 4), and 20 ng of cDNA per reaction with the StepOnePlus (Applied Biosystems). Quantitation was performed using the $\Delta\Delta C_t$ method.

Gene Expression and Survival Data Set Analysis. The Cancer Genome Atlas (TCGA) Breast Adenocarcinoma (BRCA) database (HiSeqV2, downloaded January 19, 2018 from the UCSC Xena platform (73) (https://xena.ucsc.edu)) was searched for mRNA expression and z-scores were calculated based on all tumor samples. The average z-scores for glutaminase (*GLS)*, asparagine synthetase (*ASNS)*, glutamine-fructose-6-phosphate transaminase 1 (*GFPT1*), ASCT2 (*SLC1A5*), SNAT1 (*SLC38A1*), SNAT2 (*SLC38A2*), and ATB$^{0,+}$ (*SLC6A14*) comprises the glutamine metabolism gene signature (GMGS). The average z-score of the glycolysis genes *ALDOA*, *ENO1*, *GAPDH*, *GPI*, *HK1*, *LDHA*, *PFKM*, *PFKL*, *PGAM1*, *PKM2,* and *TPI1* as well as the GLUT1 transporter (*SLC2A1*) generated the glycolysis gene signature. To avoid confounding data from highly glycolytic tumors, the basal-like breast cancer samples (PAM50) (74) with expression profiles signifying the greatest dependence on glutamine metabolism ("glutamine metabolism high") were identified based on glutamine metabolism and glycolysis gene signatures (top 12.5%). All other BLBC tumors were classified as having "mixed metabolism". A cytotoxic T lymphocyte (CTL) gene signature was calculated by averaging the z-scores of *GZMA*, *GZMB*, *PRF1*, and *IFNG* expression.

For survival analyses, the glutamine metabolism gene signature (*GLS*, 211414_at; *ASNS*, 205047_s_at; *GFPT1*, 202722_s_at; *SLC1A5*, 208916_at; *SLC38A1*, 218237_s_at; *SLC38A2*, 220924_s_at; *SLC6A14*, 219795_at) and the CTL gene signature (*GZMA*, 205488_at; *GZMB, 210164_at*; *PRF1*, 214617_at; *IFNG* 210354_at) gene expression and overall survival (OS) and distant metastasis-free survival (DMFS) data from basal breast cancer tumors were downloaded from KM plot (75) (http://www.kmplot.com). Automatic cutoff was used to define "high" versus "low" expression, with cutoff values defined as followed: *GLS* (OS: 57, range=2-587) (DMFS: 43, range=2-242), *ASNS* (OS: 1560, range=109-13370) (DMFS: 902, range=33-13370), *GFPT1* (OS: 1726, range=354-5352) (DMFS: 1138, range=377-5352), *SLC1A5* (OS: 380, range=131-2039) (DMFS: 709, range=131-2039), *SLC38A1* (OS: 3704, range=94-16075) (DMFS: 2817, range=370-14915), *SLC38A2* (OS: 2469, range=288-13482) (DMFS: 2976, range=751-7711), *SLC6A14* (OS: 899, range=1-8829) (DMFS: 920, range=3-10359), *GZMA* (OS: 239, range=17-4627) (DMFS: 272, range=46-4627), *GZMB* (OS: 289, range=7-6030) (DMFS: 295, range=18-6030), *PRF1* (OS: 201, range=46-6453) (DMFS: 203, range=56-6453), and *IFNG* (OS: 58, range=1-668) (DMFS: 68, range=2-665). Characterization of "high" expression of the CTL gene signature required "high expression" classification of at least two genes, while characterization of "high" expression of the glutamine metabolism gene signature required "high expression" classification of at least four genes. Samples were then categorized based on the glutamine metabolism gene signature or *GLS* expression and the CTL gene signature.

35

Statistics. For survival curve analysis, the Mantel-Cox method was used for log-rank analysis of all groups, with the Bonferroni correction utilized for multiple comparisons where applicable. Hazard ratios (HR) and 95% confidence intervals were calculated for single comparisons using the log rank test.

For dose response analyses, non-linear fit was applied to both CB-839 and V-9302-treated cells. To directly assess differences between CB-839 and V-9302, unpaired Student's t-test was applied at the indicated points.

All plots and statistical analyses were completed using GraphPad Prism software. Data from independent assays (dot) as well as summary data (mean with SEM) are shown. For tumor experiments, data are reported from 1-2 independent experiments, with each dot representing a single animal. For comparisons between two groups, unpaired or paired Student's *t* tests were performed as indicated. For multiple comparisons, one- or two-way analysis of variance (ANOVA) was performed with post-hoc analysis using Tukey's, Dunnett's, Holm-Sidak's, or Sidak's multiple comparisons tests, as indicated. Outliers were identified using the ROUT method (Q=5%). All statistical tests were completed as two-tailed, and $p < 0.05$ was considered statistically significant, except where corrected for multiple comparisons as indicated. All error bars are SEM.

Study approval. All mouse procedures were performed under protocols approved by Vanderbilt University's Institutional Animal Care and Utilization Committee (IACUC).

References:

1. Wise DR, Thompson CB. Glutamine addiction: a new therapeutic target in cancer. *Trends Biochem. Sci.* 2010;35(8):427–433.

2. Hensley CT, Wasti AT, DeBerardinis RJ. Glutamine and cancer: cell biology, physiology, and clinical opportunities. *J. Clin. Invest.* 2013;123(9):3678–3684.

3. O'Sullivan D, Pearce EL. Targeting T cell metabolism for therapy. *Trends Immunol.* 2015;36(2):71–80.

4. Palmer CS, Ostrowski M, Balderson B, Christian N, Crowe SM. Glucose metabolism regulates T cell activation, differentiation, and functions. *Front. Immunol.* 2015;6:1.

5. Ramsay G, Cantrell D. Environmental and metabolic sensors that control T cell biology. *Front. Immunol.* 2015;6:99.

6. Edwards DN, Ngwa VM, Wang S, et al. The receptor tyrosine kinase EphA2 promotes glutamine metabolism in tumors by activating the transcriptional coactivators YAP and TAZ. *Sci. Signal.* 2017;10(508):eaan4667.

7. Youngblood VM, Kim LC, Edwards DN, et al. The ephrin-A1/EPHA2 signaling axis regulates glutamine metabolism in HER2-positive breast cancer. *Cancer Res.* 2016;76(7):1825–1836.

8. Ngwa VM, Edwards DN, Philip M, Chen J. Microenvironmental metabolism regulates antitumor immunity. *Cancer Res.* 2019;79(16):4003–4008.

9. Nakazawa MS, Keith B, Simon MC. Oxygen availability and metabolic adaptations. *Nat. Rev. Cancer.* 2016;16(10):663–673.

10. Hanahan D, Weinberg RA. Hallmarks of cancer: The next generation. *Cell.* 2011;144(5):646–674.

11. Luo M, Brooks M, Wicha MS. Asparagine and glutamine: co-conspirators fueling metastasis. *Cell Metab.* 2018;27(5):947–949.

12. Zhang J, Pavlova NN, Thompson CB. Cancer cell metabolism: the essential role of the nonessential amino acid, glutamine. *EMBO J.* 2017;36(10):1302–1315.

13. Platten M, Nollen EAA, Röhrig UF, Fallarino F, Opitz CA. Tryptophan metabolism as a common therapeutic target in cancer, neurodegeneration and beyond. *Nat. Rev. Drug Discov.* 2019;18(5):379–401.

14. Lukey MJ, Katt WP, Cerione RA. Targeting amino acid metabolism for cancer therapy. *Drug Discov. Today.* 2017;22(5):796–804.

15. Winnike JH, Stewart DA, Pathmasiri WW, McRitchie SL, Sumner SJ. Stable isotope-resolved metabolomic differences between hormone-responsive and triple-negative breast cancer cell lines. *Int. J. Breast Cancer.* 2018;2018:2063540.

16. Altman BJ, Stine ZE, Dang CV. From Krebs to clinic: Glutamine metabolism to cancer therapy. *Nat. Rev. Cancer.* 2016;16(10):619–634.

17. Lampa M, Arlt H, He T, et al. Glutaminase is essential for the growth of triple-negative breast cancer cells with a deregulated glutamine metabolism pathway and its suppression synergizes with mTOR inhibition. *PLoS One.* 2017;12(9):e0185092.

18. Kim S, Kim DH, Jung WH, Koo JS. Expression of glutamine metabolism-related proteins according to molecular subtype of breast cancer. *Endocr. Relat. Cancer.*

2013;20(3):339–348.

19. Van Geldermalsen M, Wang Q, Nagaraha R, et al. ASCT2/SLC1A5 controls glutamine uptake and tumour growth in triple-negative basal-like breast cancer. *Oncogene.* 2016;35(24):3201–3208.

20. Wang J-B, Erickson JW, Fuji R, et al. Targeting mitochondrial glutaminase activity inhibits oncogenic transformation. *Cancer Cell.* 2010;18(3):207–219.

21. Buck MD, O'Sullivan D, Pearce EL. T cell metabolism drives immunity. *J. Exp. Med.* 2015;212(9):1345–1360.

22. Carr EL, Kelman A, Wu GS, et al. Glutamine uptake and metabolism Are coordinately regulated by ERK/MAPK during T lymphocyte activation. *J. Immunol.* 2010;185(2):1037–1044.

23. Sinclair LV, Rolf J, Emslie E, Shi YB, Taylor PM, Cantrell DA. Control of amino-acid transport by antigen receptors coordinates the metabolic reprogramming essential for T cell differentiation. *Nat. Immunol.* 2013;14(5):500–508.

24. Ron-Harel N, Ghergurovich JM, Notarangelo G, et al. T cell activation depends on extracellular alanine. *Cell Rep.* 2019; 28(12):3011-3021.e4.

25. Nakaya M, Xiao Y, Zhou X, et al. Inflammatory T cell responses rely on amino acid transporter ASCT2 facilitation of glutamine uptake and mTORC1 kinase activation. *Immunity.* 2014;40(5):692–705.

26. Johnson MO, Wolf MM, Madden MZ, et al. Distinct regulation of Th17 and Th1 cell differentiation by glutaminase-dependent metabolism. *Cell.* 2018;175(7):1780-1795.e19.

27.   Klysz D, Tai X, Robert PA, et al. Glutamine-dependent α-ketoglutarate production regulates the balance between T helper 1 cell and regulatory T cell generation. *Sci. Signal.* 2015;8(396):ra97.

28.   Siska PJ, Rathmell JC. T cell metabolic fitness in antitumor immunity. *Trends Immunol.* 2015;36(4):257–264.

29.   Cluntun AA, Lukey MJ, Cerione RA, Locasale JW. Glutamine metabolism in cancer: understanding the heterogeneity. *Trends Cancer.* 2017;3(3):169–180.

30.   O'Sullivan D, Sanin DE, Pearce EJ, Pearce EL. Metabolic interventions in the immune response to cancer. *Nat. Rev. Immunol.* 2019;19(5):324–335.

31.   Chang C-H, Qiu J, O'Sullivan D, et al. Metabolic competition in the tumor microenvironment is a driver of cancer progression. *Cell.* 2015;162(6):1229–124.

32.   Ho P-C, Bihuniak JD, Macintyre AN, et al. Phosphoenolpyruvate is a metabolic checkpoint of anti-tumor T cell responses. *Cell.* 2015;162(6):1217–1228.

33.   Bertucci F, Finetti P, Cervera N, et al. How basal are triple-negative breast cancers? *Int. J. Cancer.* 2008;123(1):236–240.

34.   Johnstone CN, Smith YE, Cao Y, et al. Functional and molecular characterisation of EO771.LMB tumours, a new C57BL/6-mouse-derived model of spontaneously metastatic mammary cancer. *Dis. Model. Mech.* 2015;8(3):237–251.

35.   Mombaerts P, Iacomini J, Johnson RS, Herrup K, Tonegawa S, Papaioannou VE. RAG-1-deficient mice have no mature B and T lymphocytes. *Cell.* 1992;68(5):869–877.

36.   Green JE, Shibata MA, Yoshidome K, et al. The C3(1)/SV40 T-antigen transgenic

mouse model of mammary cancer: ductal epithelial cell targeting with multistage progression to carcinoma. *Oncogene.* 2000;19(8):1020–1027.

37. Herschkowitz JI, Simin K, Weigman VJ, et al. Identification of conserved gene expression features between murine mammary carcinoma models and human breast tumors. *Genome Biol.* 2007;8(5):R76.

38. Deeb KK, Michalowska AM, Yoon C-Y, et al. Identification of an integrated SV40 T/t-antigen cancer signature in aggressive human breast, prostate, and lung carcinomas with poor prognosis. *Cancer Res.* 2007;67(17):8065–8080.

39. Wagner KU, Wall RJ, St-Onge L, et al. Cre-mediated gene deletion in the mammary gland. *Nucleic Acids Res.* 1997;25(21):4323–4330.

40. Heusel JW, Wesselschmidt RL, Shresta S, Russell JH, Ley TJ. Cytotoxic lymphocytes require granzyme B for the rapid induction of DNA fragmentation and apoptosis in allogeneic target cells. *Cell.* 1994;76(6):977–987.

41. Bagga P, Behar KL, Mason GF, De Feyter HM, Rothman DL, Patel AB. Characterization of cerebral glutamine uptake from blood in the mouse brain: Implications for metabolic modeling of 13C NMR data. *J. Cereb. Blood Flow Metab.* 2014;34(10):1666–1672.

42. Maggs DG, Jacob R, Rife F, et al. Interstitial fluid concentrations of glycerol, glucose, and amino acids in human quadricep muscle and adipose tissue: evidence for significant lipolysis in skeletal muscle. *J. Clin. Invest.* 1995;96(1):370–377.

43. Kew S, Wells SM, Yaqoob P, Wallace FA, Miles EA, Calder PC. Dietary glutamine

enhances murine T-lymphocyte responsiveness. *J. Nutr.* 1999;129(8):1524–1531.

44. Rötzschke O, Falk K, Stevanovic S, Jung G, Walden P, Rammensee H-G. Exact prediction of a natural T cell epitope. *Eur. J. Immunol.* 1991;21(11):2891–2894.

45. Hogquist KA, Jameson SC, Heath WR, Howard JL, Bevan MJ, Carbone FR. T cell receptor antagonist peptides induce positive selection. *Cell.* 1994;76(1):17–27.

46. Carbone FR, Sterry SJ, Butler J, Rodda S, Moore MW. T cell receptor α-chain pairing determines the specificity of residue 262 within the kb-restricted, ovalbumin257-264 determinant. *Int. Immunol.* 1992;4(8):861–867.

47. Parlati F. Anti-tumor acitivity of glutaminase inhibitor CB-839 in combination with clinical anti-cancer agents. Presented at: Keystone Symposium on Tumor Metababolism; January 21-25, 2018; Snowbird, UT, USA.

48. Schulte ML, Fu A, Zhao P, et al. Pharmacological blockade of ASCT2-dependent glutamine transport leads to antitumor efficacy in preclinical models. *Nat. Med.* 2018;24(2):194–202.

49. Bröer A, Fairweather S, Bröer S. Disruption of amino acid homeostasis by novel ASCT2 inhibitors involves multiple targets. *Front. Pharmacol.* 2018;9:785.

50. Ayers M, Lunceford J, Nebozhyn M, et al. IFN-γ-related mRNA profile predicts clinical response to PD-1 blockade. *J. Clin. Invest.* 2017;127(8):2930–2940.

51. Lohneis P, Sinn M, Bischoff S, et al. Cytotoxic tumour-infiltrating T lymphocytes influence outcome in resected pancreatic ductal adenocarcinoma. *Eur. J. Cancer.* 2017;83:290–301.

52. Peranzoni E, Lemoine J, Vimeux L, et al. Macrophages impede CD8 T cells from

reaching tumor cells and limit the efficacy of anti–PD-1 treatment. *Proc. Natl. Acad. Sci. U. S. A.* 2018;115(17):E4041–E4050.

53.   Klebanoff CA, Gattinoni L, Torabi-Parizi P, et al. Central memory self/tumor-reactive CD8+ T cells confer superior antitumor immunity compared with effector memory T cells. *Proc. Natl. Acad. Sci. U. S. A.* 2005;102(27):9571–9576.

54.   Klebanoff CA, Finkelstein SE, Surman DR, et al. IL-15 enhances the in vivo antitumor activity of tumor-reactive CD8 + T Cells. *Proc. Natl. Acad. Sci. U. S. A.* 2004;101(7):1969–1974.

55.   Delgoffe GM, Kole TP, Zheng Y, et al. The mTOR kinase differentially regulates effector and regulatory T cell lineage commitment. *Immunity.* 2009;30(6):832–844.

56.   Powell JD, Lerner CG, Schwartz RH. Inhibition of cell cycle progression by rapamycin induces T cell clonal anergy even in the presence of costimulation. *J. Immunol.* 1999;162(5):2775–2784.

57.   Kim CS, Cho SH, Chun HS, et al. BCH, an inhibitor of system L amino acid transporters, induces apoptosis in cancer cells. *Biol. Pharm. Bull.* 2008;31(6):1096–1100.

58.   Sloan JL, Mager S. Cloning and functional expression of a human Na+ and Cl--dependent neutral and cationic amino acid transporter B0+. *J. Biol. Chem.* 1999;274(34):23740–23745.

59.   Marra A, Viale G, Curigliano G. Recent advances in triple negative breast cancer: the immunotherapy era. *BMC Med.* 2019;17(1):90.

60.   Wang M, Zhao J, Zhang L, et al. Role of tumor microenvironment in

tumorigenesis. *J. Cancer.* 2017;8(5):761–773.

61.   Balkwill FR, Capasso M, Hagemann T. The tumor microenvironment at a glance. *J. Cell Sci.* 2012;125(23):5591–5596.

62.   Palmieri EM, Menga A, Martin-Perez R, et al. Pharmacologic or genetic targeting of glutamine synthetase skews macrophages toward an M1-like phenotype and inhibits tumor metastasis. *Cell Rep.* 2017;20(7):1654–1666.

63.   Rohlenova K, Veys K, Miranda-Santos I, De Bock K, Carmeliet P. Endothelial cell metabolism in health and disease. *Trends Cell Biol.* 2018;28(3):224–236.

64.   Liu PS, Wang H, Li X, et al. α-ketoglutarate orchestrates macrophage activation through metabolic and epigenetic reprogramming. *Nat. Immunol.* 2017;18(9):985–994.

65.   Oh MH, Sun IH, Zhao L, et al. Targeting glutamine metabolism enhances tumor-specific immunity by modulating suppressive myeloid cells. *J. Clin. Invest.* 2020;130(7):3865–3884.

66.   Suzuki J, Yamada T, Inoue K, et al. The tumor suppressor menin prevents effector CD8 T-cell dysfunction by targeting mTORC1-dependent metabolic activation. *Nat. Commun.* 2018;9(1):3296.

67.   Nabe S, Yamada T, Suzuki J, et al. Reinforce the antitumor activity of CD8+ T cells via glutamine restriction. *Cancer Sci.* 2018;109(12):3737–3750.

68.   Masle-Farquhar E, Bröer A, Yabas M, Enders A, Bröer S. ASCT2 (SLC1A5)-deficient mice have normal B-cell development, proliferation, and antibody production. *Front. Immunol.* 2017;8:549.

69. Matheson NJ, Sumner J, Wals K, et al. Cell surface proteomic map of HIV infection reveals antagonism of amino acid metabolism by Vpu and Nef. *Cell Host Microbe.* 2015;18(4):409–423.

70. Leone RD, Zhao L, Englert JM, et al. Glutamine blockade induces divergent metabolic programs to overcome tumor immune evasion. *Science.* 2019;366(6468):1013–1021.

71. Wiig H, Aukland K, Tenstad O. Isolation of interstitial fluid from rat mammary tumors by a centrifugation method. *Am. J. Physiol. Heart Circ. Physiol.* 2003;284(1):H416–H424.

72. Kemp RA, Ronchese F. Tumor-specific Tc1, but not Tc2, cells deliver protective antitumor immunity. *J. Immunol.* 2001;167(11):6497–6502.

73. Goldman MJ, Craft B, Hastie M, et al. Visualizing and interpreting cancer genomics data via the Xena platform. *Nat. Biotechnol.* 2020;38(6):675–678.

74. Network TCGA, Comprehensive molecular portraits of human breast tumours. *Nature.* 2012;490(7418):61–70.

75. Nagy Á, Lánczky A, Menyhárt O, Gyorffy B. Validation of miRNA prognostic power in hepatocellular carcinoma using expression data of independent datasets. *Sci. Rep.* 2018;8(1):9227.

Figure Legends:

Figure 1. Glutamine metabolism inversely correlates with expression of T cell activation markers in glutamine metabolism high human basal-like breast cancer samples. (**A-C**) Analysis of mRNA expression ($\log_2$) *z*-scores in basal-like tumor samples from the TCGA BRCA dataset. The samples with the greatest glutamine metabolism gene signature combined with the lowest glycolysis gene signature are considered "glutamine metabolism high". All others are considered to have "mixed metabolism". (**A**) Expression levels of individual genes are displayed as a heat map, with low expression in blue and high expression in red. (**B-C**) The CTL gene signature [*GZMA+GZMB+PRF1+INFG*)/4] was plotted as a function of the glutamine metabolism gene signature (GMGS) or *GLS* for basal-like breast cancer samples that are "glutamine metabolism high" (black) and "mixed metabolism" (pink). Linear regression lines of best fit are shown for both groups. Pearson correlation analyses are shown. (**D**) Kaplan-Meier analysis of overall survival of basal breast tumors stratified based on the glutamine metabolism gene signature (GMGS) and the CTL gene signature (GMGS^{LOW}/CTL^{HIGH} (green, n=64), GMGS^{LOW}/CTL^{LOW} (blue, n=14), GMGS^{HIGH}/CTL^{HIGH} (orange, n=121), and GMGS^{HIGH}/CTL^{LOW} (red, n=42)). Log rank (Mantel-Cox) test with p-values are shown. Red box indicates statistical significance after Bonferroni correction for multiple comparisons. Hazard ratio (HR) (logrank) and 95% confidence intervals are shown.

Figure 2. Loss of tumor cell-specific GLS reduces tumor growth and metastasis in a lymphocyte-dependent manner in an orthotopic model of TNBC. (**A-D**) E0771

47

sgLacZ (E0771-WT, red) or sgGls_3C15 (E0771-GLS^{KO}, blue) (5x10^5) cells were

implanted into the #4 mammary fat pad of female C57BL/6 mice (Jackson Laboratories),

and tumors were harvested after 14 days. (**A**) Tumor volume (two-way ANOVA;

p=1.19x10^{-10}) and (**B**) tumor weight at harvest (unpaired Student's t-test; p=7.94x10^{-4})

are shown. n=5 mice per group. (**C-D**) Tumor sections from (*A-B*) were stained by (**C**)

immunohistochemistry for GLS (brown) or immunofluorescence for (**D**) Ki67 (red).

Nuclei were stained with (*C*) hematoxylin (blue) or (*D*) DAPI (blue). Total nuclei and

Ki67$^+$ cells were counted from three fields of view using ImageJ software. Scale bars

are 10 μm (GLS) or 20μm (Ki67). Unpaired Student's t-test; p=0.84. n=3 mice per

group. (**E-G**) E0771-WT or E0771-GLS^{KO} cells were implanted as described above in

wild-type C57BL/6 (*Rag1$^{+/+}$)* or Rag1-deficient (*Rag1$^{-/-}$*) mice. (**E**) Plot of tumor volumes

is shown. Two-way ANOVA (p=2.66x10^{-6}) was performed. (**F**) Image of tumors

harvested from (*E*). n=4 mice per group. (**G**) Immunofluorescence of cleaved caspase-3

(red). Nuclei were stained with DAPI (blue). One-way ANOVA (p=0.011) was

performed Tukey's post-hoc analysis for multiple comparisons. n=3 mice per group. (**H-
I**) C57BL/6 (*Rag1$^{+/+}$*) (**H**) or *Rag1$^{-/-}$* (**I**) mice were implanted with E0771-WT or E0771-

GLS^{KO} cells (2.5x10^5). (**H**) Lungs were harvested when tumors reached 400-600 mm^3

(21-27 days). Micrometastases (black arrows) were scored from three H&E sections

isolated 100μm apart (n=4 mice per group). Scale bar is 200 μm. (**I**) Tumors were

resected at 1400-1500 mm^3, and lungs were harvested between 13 and 20 days post

resection (n=5 mice per group). Surface metastases (yellow arrows) were scored from

whole lung specimens. Unpaired Student's t-test; (*H*) p=0.031, (*I*) p=0.062. *p<0.05, **p<0.01, ***p<0.005, ****p<0.001.

Figure 3. Mammary-specific loss of GLS in a spontaneous TNBC tumor model delays tumor initiation and improves activation of T cells. *C3(1)-TAg/GLS$^{FL/FL}$ (GLS$^{FL/FL}$*, red) or *C3(1)-TAg; MMTV-Cre; GLS$^{FL/FL}$ (GLS$^{\Delta/\Delta}$*, blue) mice were palpitated weekly for tumor formation and progression. (**A**) Tumor latency for *GLS$^{FL/FL}$* or *GLS$^{\Delta/\Delta}$* mice was recorded as the age (weeks) of initial tumor detection. Unpaired Student's t-test; p=0.031. n=11-12 mice per group. (**B**) Survival (weeks) was determined by the humane endpoint for the *GLS$^{FL/FL}$* or *GLS$^{\Delta/\Delta}$* from (*A*), plotted as the percent (%) of surviving mice as a function of age (weeks). Gehan-Breslow-Wilcoxon test; p=0.0082. Hazard ratio was calculated using logrank analysis, with the 95% confidence interval shown. (**C**) Plot of tumor volume after tumor initiation in mice described in (*A*). (**D**) H&E images of *GLS$^{FL/FL}$* or *GLS$^{\Delta/\Delta}$* tumors. Scale bars are 200 μm (top) or 100 μm (bottom). (**E**) Immunohistochemistry for GLS (brown) of *GLS$^{FL/FL}$* or *GLS$^{\Delta/\Delta}$* tumors. Nuclei were stained with hematoxylin (blue). Scale bar is 20 μm. (**F**) Tumors were harvested from *GLS$^{FL/FL}$* (red) or *GLS$^{\Delta/\Delta}$* (blue) mice at 1-2 weeks post initial tumor detection. Tumor volume (mm^3) (left) and tumor mass (grams) (right) were recorded at harvest. Unpaired Student's t-test; p=0.581 (volume), p=0.581 (mass). n=7-9 mice per group. (**G-N**) Flow cytometric analyses of whole tumor preparations. n=5-6 mice per group. (**G**) CD4$^+$ (left) or CD8$^+$ (right) T cells, plotted as percentage of CD45$^+$ immune cells. Unpaired Student's t-test; p=0.226 (CD4$^+$), p=0.043 (CD8$^+$). (**H-N**) Flow cytometric analyses of

49

(**H**) CD8$^+$GZMB$^+$, (**I**) CD8$^+$CD107a$^+$, (**J**) CD8$^+$IFNγ$^+$, (**K**) CD4$^+$IFNγ$^+$, (**L**) CD4$^+$IL-4$^+$, (**M**)

CD4$^+$IL-17A$^+$, and (**N**) CD4$^+$FoxP3$^+$ T cells in GLS$^{FL/FL}$ (red) or GLS$^{Δ/Δ}$ (blue) tumors,

plotted as a percentage (%) of CD45$^+$ cells. Unpaired Student's t test; p=0.0085

(CD8$^+$GZMB$^+$), p=0.0056 (CD8$^+$CD107a$^+$), p=4.94x10^{-5} (CD8$^+$IFNγ$^+$), p=0.011

(CD4$^+$IFNγ$^+$), p=0.212 (CD4$^+$IL-4$^+$), p=0.322 (CD4$^+$IL-17A$^+$), p=0.093 (CD4$^+$FoxP3$^+$).

*p<0.05, **p<0.01, ****p<0.001.

**Figure 4. Loss of tumor cell-specific GLS increases T cell activation in an
orthotopic TNBC tumor model.** (**A-I**) E0771 sgLacZ (WT, red) or sgGls_3C15

(GLS^{KO}, blue) (5x10^5) cells were implanted into the #4 mammary fat pad of female

C57BL/6 mice (Jackson Laboratories). Tumors were harvested after 14 days. n=4-5

mice per group. (**A-B**) Flow cytometric analyses of CD4$^+$ (left) or CD8$^+$ (right) T cells,

plotted as percentage of (**A**) CD45$^+$ immune cells or (**B**) total cells normalized to tumor

mass (gram). Unpaired Student's t-test; CD4$^+$, (*A*) p=0.091, (*B*) p=0.0063; CD8$^+$, (*A*)

p=0.040, (B) p=8.23x10^{-4}. (**C-I**) Flow cytometric analyses of tumors for (**C**)

CD8$^+$GZMB$^+$, (**D**) CD8$^+$CD107a$^+$, (**E**) CD8$^+$IFNγ$^+$, (**F**) CD4$^+$IFNγ$^+$, (**G**) CD4$^+$IL-4$^+$, (**H**)

CD4$^+$IL-17A$^+$, and (**I**) CD4$^+$FoxP3$^+$ CD45$^+$CD3$^+$ T cells. Total counts were normalized

per tumor mass (gram). Unpaired Student's t-test; p=0.0064 (CD8$^+$GZMB$^+$), p=0.027

(CD8$^+$CD107a$^+$), p=0.0091 (CD8$^+$IFNγ$^+$), p=0.0065 (CD4$^+$IFNγ$^+$), p=0.065 (CD4$^+$IL-4$^+$),

p=0.017 (CD4$^+$IL-17A$^+$), p=0.198 (CD4$^+$FoxP3$^+$). (**J**) Tumor interstitial fluid was collected

from E0771-WT (red) or E0771-GLS^{KO} (blue) tumors via centrifugation of harvested

tumors. Glutamine (gln) was measured and concentration (μM) was calculated against

a glutamine standard. Paired Student's t-test; p=0.021. n=5 mice per group. (**K**) IFNγ

ELISA of supernatants collected from Tc1 CD8$^+$ T cells activated (αCD3/αCD28) in

media supplemented with 0.1, 0.5, or 2 mM glutamine (n=3). Two-way ANOVA;

unpaired Student's t-test. (**L-N**) E0771(OVA) sgLacZ (WT, red) or sgGls3 (GLS^{KO}, blue)

(5x10^5) cells were bilaterally implanted into the #4 mammary fat pads of female

C57BL/6 mice. (**L**) Experimental timeline is shown. (**M**) Immunofluorescence of

GFP$^+$CD8$^+$ OT-I (GFP$^+$CTLs) cells in tumors. Nuclei were stained with DAPI (blue).

Arrows indicate GFP$^+$CD8$^+$ OT-I T cells. Scale bar is 20 μm. (**N**) Flow cytometric

analysis of of GFP$^+$CD8$^+$ T cells from whole cell tumor preparations, plotted as

percentage of all live cells. Unpaired Student's t-test; p=0.043. n=3-4 mice per group.

*p<0.05, **p<0.01, ***p<0.005.

Figure 5. The glutamine transporter inhibitor V-9302 suppresses tumor growth

and increases T lymphocyte activation in a model of TNBC. E0771 cells (2.5x10^5)

were bi-laterally injected into the #4 mammary fat pads of female C57BL/6 mice

(Taconic). Beginning at day 11, mice were treated with vehicle (DMSO, red) or 50 mg/kg

V-9302 (blue) daily for 5 days. (**A**) Tumor volume was measured over time. Arrow

indicates beginning of treatment. Two-way ANOVA; p<1x10^{-15}. n=9-10 mice per group.

(**B**) Average tumor mass per mouse at harvest. Unpaired Student's t-test; p=0.0060.

n=9-10 mice per group. (**C**) Immunofluorescence of tumor sections for Ki67 (top) or

cleaved caspase-3 (bottom), both red. Nuclei were stained with DAPI (blue). Scale bar

is 20 μm. Ki67$^+$, cleaved caspase-3$^+$, and nuclei were averaged from three fields of

view. Unpaired Student's t-test; p=0.283 (Ki67), p=0.023 (Cl. Casp-3). (**D**) Flow

cytometric analyses of CD4$^+$ (left) or CD8$^+$ (right) T cells, plotted as a percentage (%) of

CD45$^+$ immune cells, in vehicle- (red) or V-9302-treated (blue) tumors. Unpaired

Student's t test; p=0.023 (CD4$^+$), p=0.340 (CD8$^+$). n=5 mice per group. (**E**)

Immunohistochemistry of CD8a (brown) from vehicle or V-9302-treated (50 mg/kg)

tumors. Nuclei were stained with hematoxylin (blue). Edge (black) is considered

<500μm (denoted by solid line) from tumor margin, core (red) is >500μm. Scale bars

are 500μm and 50μm for expanded or enlarged images, respectively. CD8$^+$ cells

(denoted by arrows) were averaged from three fields of view and normalized to field-of-

view area. Unpaired Student's t-test; p=0.019. n=3 mice per group. (**F-K**) Flow

cytometric analyses of (**F**) CD8$^+$GZMB$^+$, (**G**) CD8$^+$CD107a$^+$, (**H**) CD8$^+$IFNγ$^+$, (**I**)

CD4$^+$IFNγ$^+$, (**J**) CD4$^+$IL-4$^+$, and (**I**) CD4$^+$FoxP3$^+$CD25$^+$CD127^{lo} CD45$^+$CD3$^+$ T cells in

vehicle (red) or V-9302-treated (blue) tumors. Unpaired Student's t-test; p=0.014

(CD8$^+$GZMB$^+$), p=0.047 (CD8$^+$CD107a$^+$), p=0.007 (CD8$^+$IFNγ$^+$), p=0.0021 (CD4$^+$IFNγ$^+$),

p=0.057 (CD4$^+$IL-4$^+$), p=0.034 (CD4$^+$FoxP3$^+$CD25$^+$CD127^{lo}). n=3-8 mice per group.

*p<0.05, **p<0.01, ****p<0.001.

Figure 6. V-9302 induces ATB$^{0,+}$ expression to sustain glutamine uptake and

glutathione synthesis in activated CD8$^+$ T cells. (**A**) LDH cytotoxicity of E0771(OVA)

and CD8$^+$ OT-I CTLs co-cultured in vehicle (red) or V-9302 (blue) (n=3). One-way

ANOVA (p=0.0018), Tukey's post-hoc. (**B**) Tumor interstitial fluid glutamine in vehicle or

V-9302-treated tumors. Unpaired Student's t-test; p=0.0027. n=6 mice per group. (**C-D**)

^{3}H-glutamine uptake assay in (**C**) E0771 and C567BL/6 CD8$^+$ CTLs or (**D**) HCC1806 and human CD8$^+$ CTLs isolated from PBMCs in vehicle or V-9302 (n=3-4). Averaged triplicate radioactivity (CPM) was normalized to vehicle. Two-way ANOVA (E0771: $p=2.18 \times 10^{-4}$; HCC1806: $p=1.43 \times 10^{-4}$), Tukey's post-hoc. (**E**) Relative expression of ATB$^{0,+}$/*Slc6a14* (n=3). Two-way ANOVA (p=0.036), Tukey's post-hoc. (**F**) ATB$^{0,+}$ western blot of cells from (*E*). Relative ATB$^{0,+}$ protein was normalized as indicated (n=3). Two-way ANOVA (bottom, p=0.0014; right, p=0.0026), Tukey's (bottom) or Sidak's (right) post-hoc. (**G-H**) ^{3}H-glutamine uptake of CD8$^+$ CTLs (**G**) after *ATB$^{0,+}$* knockdown or (**H**) in the presence of glutamine transporter inhibitors, as indicated (n=4). One-way ANOVA ((G): $p=4.98 \times 10^{-5}$; (H): $p=3.41 \times 10^{-4}$), Holm-Sidak post-hoc. (**I-J**) CD8$^+$ CTLs overexpressing ATB$^{0,+}$ were evaluated for (**I**) ^{3}H-glutamine uptake or (**J**) LDH cytotoxicity (n=3-4). Empty vector (EV) was used as a control. (*I*) Unpaired Student's t-test ($p=7.39 \times 10^{-4}$). (*J*) One-way ANOVA ($p=4.13 \times 10^{-5}$), Tukey's post-hoc. (**K-L**) Intracellular (**K**) GSH and (**L**) cysteine in CD8$^+$ CTLs (n=4-5). Paired (p=0.020) (*K*) or unpaired (p=0.027) (*L*) Student's t-test. (**M**) xCT/*Slc7a11* expression in activated CD8$^+$ CTLs (n=3). Unpaired Student's t-test, p=0.025. (**N**) GCLC protein expression in CD8$^+$ TILs in tumors of vehicle or V-9302-treated mice. Dotted line denotes vehicle peak in representative data shown. Unpaired Student's t-test, p=0.0034. n=7 mice per group. (**O**) ROS in activated CD8$^+$CD44$^+$CD62L$^-$ effector T cells by DCF (n=4). Unpaired Student's t-test, p=0.016. (**P**) Proposed model of V-9302-mediated increases (bold) and decreases (gray) in CD8$^+$ TILs. *p<0.05, **p<0.01, ***p<0.005, ****p<0.001.
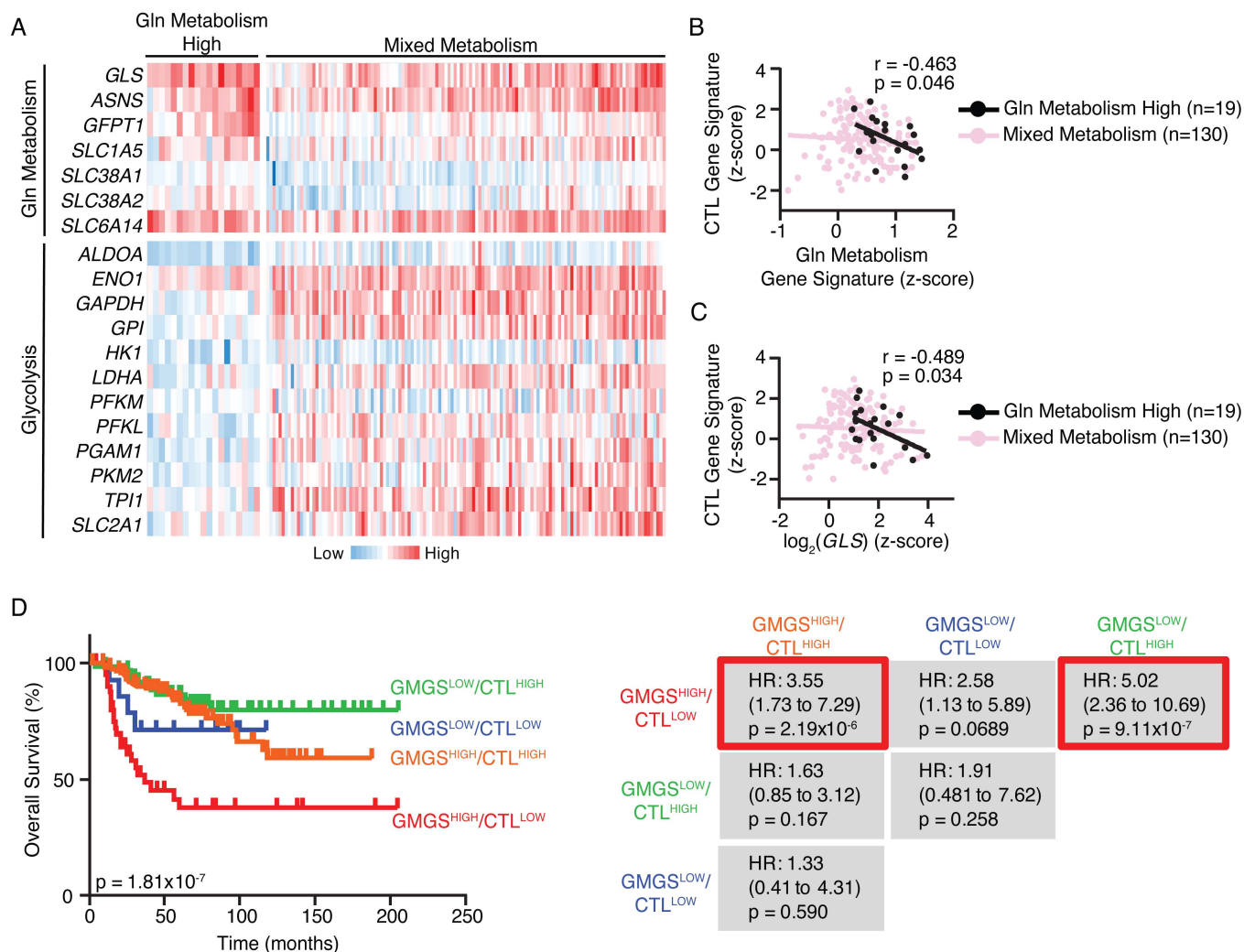
Figure 1. Glutamine metabolism inversely correlates with expression of T cell activation markers in glutamine metabolism high human basal-like breast cancer samples. (**A-C**) Analysis of mRNA expression ($\log_2$) z-scores in basal-like tumor samples from the TCGA BRCA dataset. The samples with the greatest glutamine metabolism gene signature combined with the lowest glycolysis gene signature are considered "glutamine metabolism high". All others are considered to have "mixed metabolism". (**A**) Expression levels of individual genes are displayed as a heat map, with low expression in blue and high expression in red. (**B-C**) The CTL gene signature [*GZMA+GZMB+PRF1+INFG*)/4] was plotted as a function of the glutamine metabolism gene signature (GMGS) or GLS for basal-like breast cancer samples that are "glutamine metabolism high" (black) and "mixed metabolism" (pink). Linear regression lines of best fit are shown for both groups. Pearson correlation analyses are shown. (**D**) Kaplan-Meier analysis of overall survival of basal breast tumors stratified based on the glutamine metabolism gene signature (GMGS) and the CTL gene signature (GMGS^{LOW}/CTL^{HIGH} (green, n=64), GMGS^{LOW}/CTL^{LOW} (blue, n=14), GMGS^{HIGH}/CTL^{HIGH} (orange, n=121), and GMGS^{HIGH}/CTL^{LOW} (red, n=42). Log rank (Mantel-Cox) test with p-values are shown. Red box indicates statistical significance after Bonferroni correction for multiple comparisons. Hazard ratio (HR) (logrank) and 95% confidence intervals are shown.
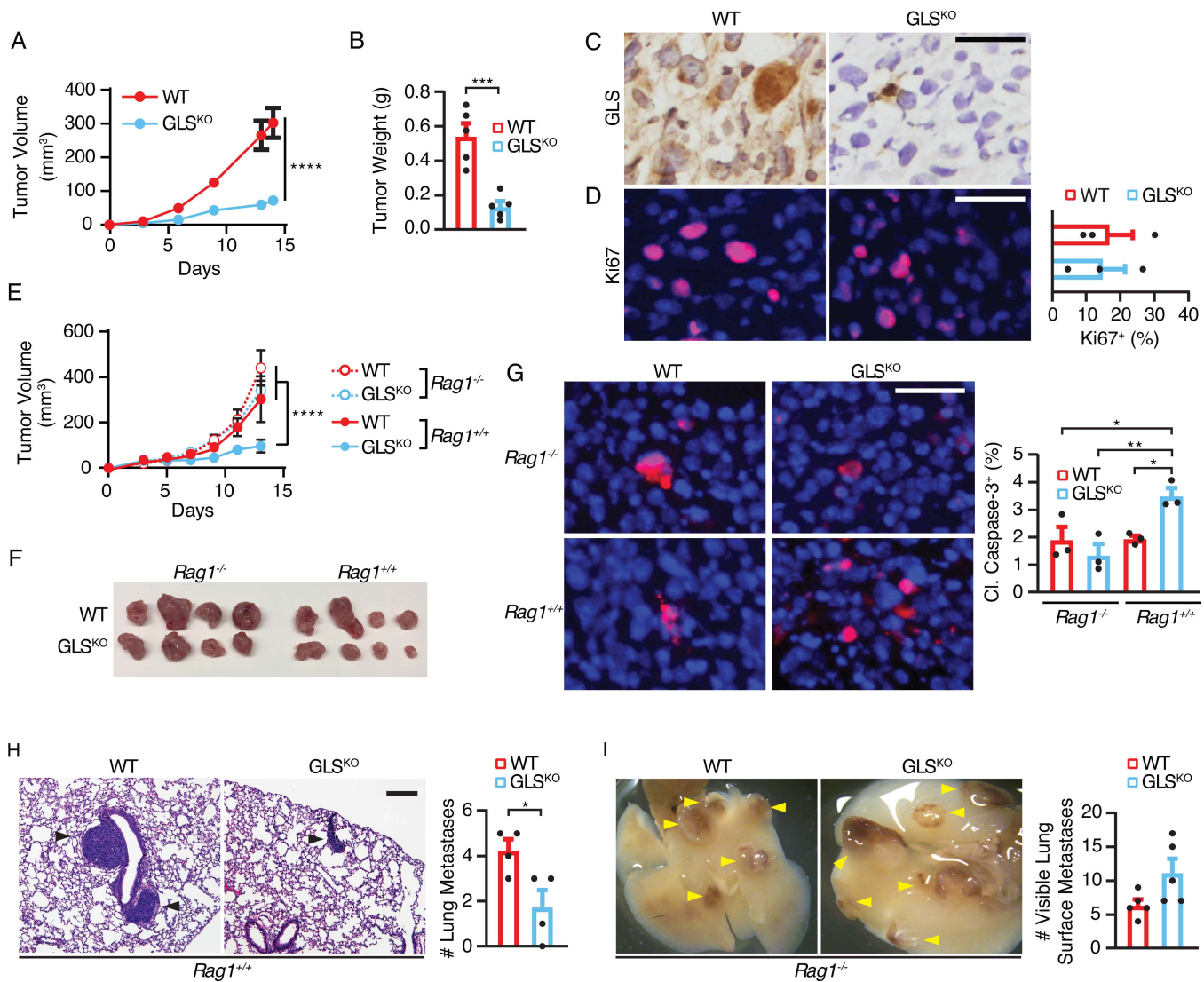
Figure 2. Loss of tumor cell-specific GLS reduces tumor growth and metastasis in a lymphocyte-dependent manner in an orthotopic model of TNBC. (**A-D**) E0771 sgLacZ (E0771-WT, red) or sgGls_3C15 (E0771-GLS^{KO}, blue) (5×10^5) cells were implanted into the #4 mammary fat pad of female C57BL/6 mice (Jackson Laboratories), and tumors were harvested after 14 days. (**A**) Tumor volume (two-way ANOVA; p=1.19×10^{-10}) and (**B**) tumor weight at harvest (unpaired Student's t-test; p=7.94×10^{-4}) are shown. n=5 mice per group. (**C-D**) Tumor sections from (*A-B*) were stained by (**C**) immunohistochemistry for GLS (brown) or immunofluorescence for (**D**) Ki67 (red). Nuclei were stained with (*C*) hematoxylin (blue) or (*D*) DAPI (blue). Total nuclei and Ki67$^+$ cells were counted from three fields of view using ImageJ software. Scale bars are 10μm (GLS) or 20μm (Ki67). Unpaired Student's t-test; p=0.84. n=3 mice per group. (**E-G**) E0771-WT or E0771-GLS^{KO} cells were implanted as described above in wild-type C57BL/6 (*Rag1$^{+/+}$*) or Rag1-deficient (*Rag1$^{-/-}$*) mice. (**E**) Plot of tumor volumes is shown. Two-way ANOVA (p=2.66×10^{-6}) was performed. (**F**) Image of tumors harvested from (*E*). n=4 mice per group. (**G**) Immunofluorescence of cleaved caspase-3 (red). Nuclei were stained with DAPI (blue). One-way ANOVA (p=0.011) was performed Tukey's post-hoc analysis for multiple comparisons. n=3 mice per group. (**H-I**) C57BL/6 (*Rag1$^{+/+}$*) (**H**) or *Rag1$^{-/-}$* (**I**) mice were implanted with E0771-WT or E0771-GLS^{KO} cells (2.5×10^5). (**H**) Lungs were harvested when tumors reached 400-600 mm^3 (21-27 days). Micrometastases (black arrows) were scored from three H&E sections isolated 100μm apart (n=4 mice per group). Scale bar is 200 μm. (**I**) Tumors were resected at 1400-1500 mm^3, and lungs were harvested between 13 and 20 days post resection (n=5 mice per group). Surface metastases (yellow arrows) were scored from whole lung specimens. Unpaired Student's t-test; (*H*) p=0.031, (*I*) p=0.062. *p<0.05, **p<0.01, ***p<0.005, ****p<0.001.
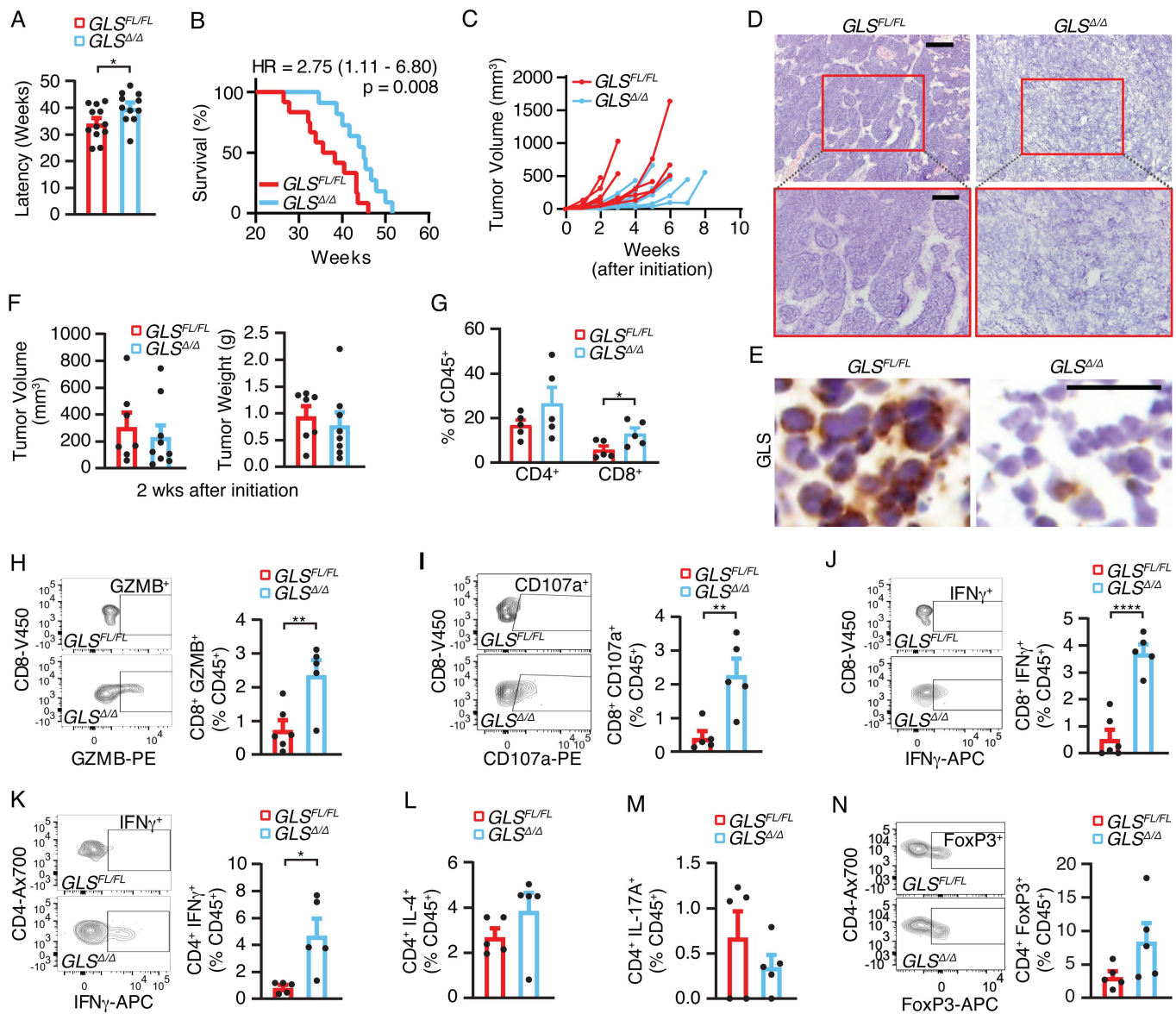
Figure 3. Mammary-specific loss of GLS in a spontaneous TNBC tumor model delays tumor initiation and improves activation of T cells. *C3(1)-TAg/GLS^{FL/FL}* (*GLS^{FL/FL}*, red) or *C3(1)-TAg; MMTV-Cre; GLS^{FL/FL}* (*GLS^{Δ/Δ}*, blue) mice were palpitated weekly for tumor formation and progression. (**A**) Tumor latency for *GLS^{FL/FL}* or *GLS^{Δ/Δ}* mice was recorded as the age (weeks) of initial tumor detection. Unpaired Student's t-test; p=0.031. n=11-12 mice per group. (**B**) Survival (weeks) was determined by the humane endpoint for the *GLS^{FL/FL}* or *GLS^{Δ/Δ}* from (*A*), plotted as the percent (%) of surviving mice as a function of age (weeks). Gehan-Breslow-Wilcoxon test; p=0.0082. Hazard ratio was calculated using logrank analysis, with the 95% confidence interval shown. (**C**) Plot of tumor volume after tumor initiation in mice described in (*A*). (**D**) H&E images of *GLS^{FL/FL}* or *GLS^{Δ/Δ}* tumors. Scale bars are 200 μm (top) or 100 μm (bottom). (**E**) Immunohistochemistry for GLS (brown) of *GLS^{FL/FL}* or *GLS^{Δ/Δ}* tumors. Nuclei were stained with hematoxylin (blue). Scale bar is 20 μm. (**F**) Tumors were harvested from *GLS^{FL/FL}* (red) or *GLS^{Δ/Δ}* (blue) mice at 1-2 weeks post initial tumor detection. Tumor volume (mm^3) (left) and tumor mass (grams) (right) were recorded at harvest. Unpaired Student's t-test; p=0.581 (volume), p=0.581 (mass). n=7-9 mice per group. (**G-N**) Flow cytometric analyses of whole tumor preparations. n=5-6 mice per group. (**G**) CD4$^+$ (left) or CD8$^+$ (right) T cells, plotted as percentage of CD45$^+$ immune cells. Unpaired Student's t-test; p=0.226 (CD4$^+$), p=0.043 (CD8$^+$). (**H-N**) Flow cytometric analyses of (**H**) CD8$^+$GZMB$^+$, (**I**) CD8$^+$CD107a$^+$, (**J**) CD8$^+$IFNγ$^+$, (**K**) CD4$^+$IFNγ$^+$, (**L**) CD4$^+$IL-4$^+$, (**M**) CD4$^+$IL-17A$^+$, and (**N**) CD4$^+$FoxP3$^+$ T cells in GLS$^{FL/FL}$ (red) or GLS$^{Δ/Δ}$ (blue) tumors, plotted as a percentage (%) of CD45$^+$ cells. Unpaired Student's t test; p=0.0085 (CD8$^+$GZMB$^+$), p=0.0056 (CD8$^+$CD107a$^+$), p=4.94x10^{-5} (CD8$^+$IFNγ$^+$), p=0.011 (CD4$^+$IFNγ$^+$), p=0.212 (CD4$^+$IL-4$^+$), p=0.322 (CD4$^+$IL-17A$^+$), p=0.093 (CD4$^+$FoxP3$^+$). *p<0.05, **p<0.01, ****p<0.001.
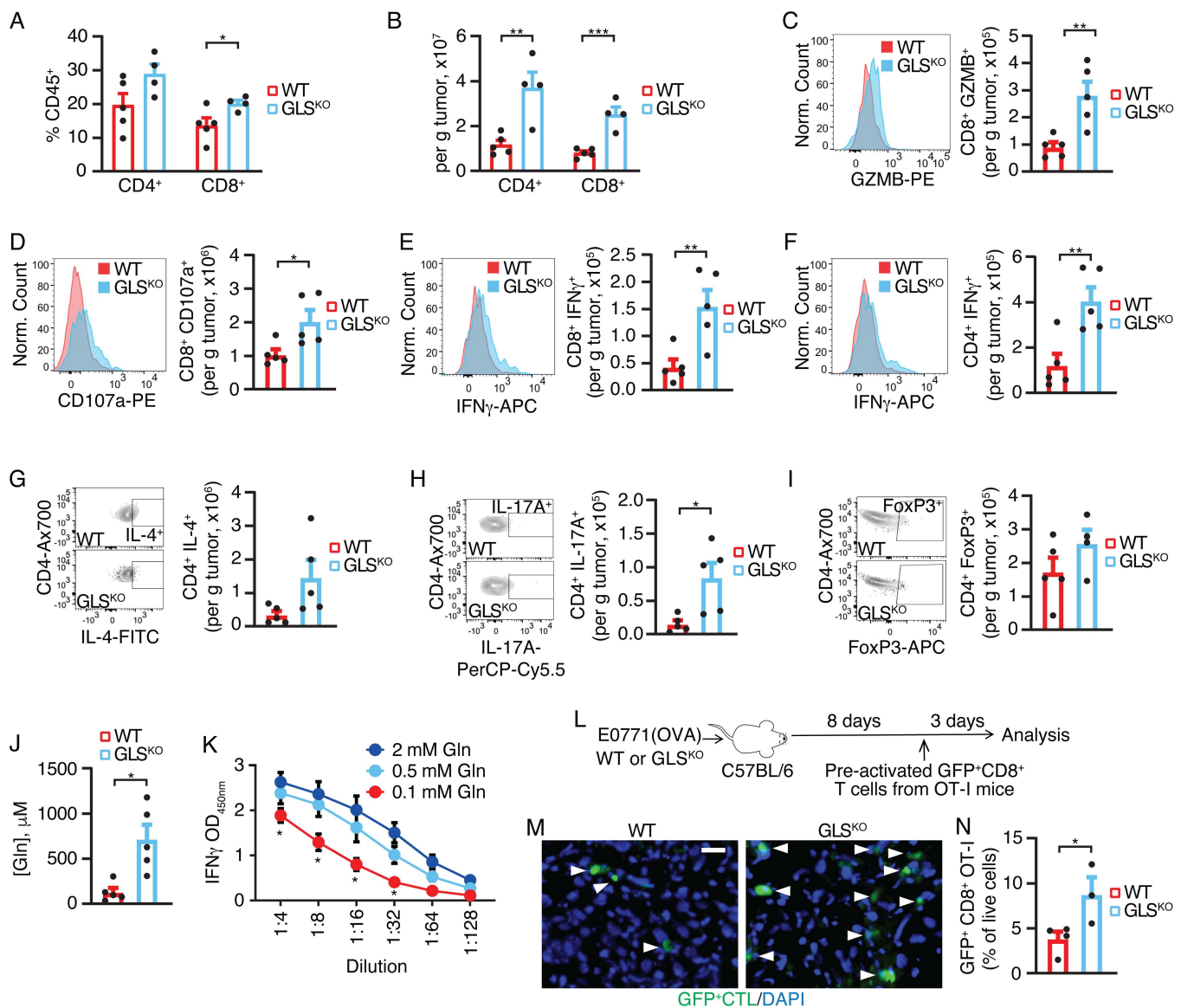
Figure 4. Loss of tumor cell-specific GLS increases T cell activation in an orthotopic TNBC tumor model. (**A-I**) E0771 sgLacZ (WT, red) or sgGls_3C15 (GLS^KO, blue) (5x10^5) cells were implanted into the #4 mammary fat pad of female C57BL/6 mice (Jackson Laboratories). Tumors were harvested after 14 days. n=4-5 mice per group. (**A-B**) Flow cytometric analyses of CD4$^+$ (left) or CD8$^+$ (right) T cells, plotted as percentage of (**A**) CD45$^+$ immune cells or (**B**) total cells normalized to tumor mass (gram). Unpaired Student's t-test; CD4$^+$, (*A*) p=0.091, (*B*) p=0.0063; CD8$^+$, (*A*) p=0.040, (B) p=8.23x10^{-4}. (**C-I**) Flow cytometric analyses of tumors for (**C**) CD8$^+$GZMB$^+$, (**D**) CD8$^+$CD107a$^+$, (**E**) CD8$^+$IFNγ$^+$, (**F**) CD4$^+$IFNγ$^+$, (**G**) CD4$^+$IL-4$^+$, (**H**) CD4$^+$IL-17A$^+$, and (**I**) CD4$^+$FoxP3$^+$ CD45$^+$CD3$^+$ T cells. Total counts were normalized per tumor mass (gram). Unpaired Student's t-test; p=0.0064 (CD8$^+$GZMB$^+$), p=0.027 (CD8$^+$CD107a$^+$), p=0.0091 (CD8$^+$IFNγ$^+$), p=0.0065 (CD4$^+$IFNγ$^+$), p=0.065 (CD4$^+$IL-4$^+$), p=0.017 (CD4$^+$IL-17A$^+$), p=0.198 (CD4$^+$FoxP3$^+$). (**J**) Tumor interstitial fluid was collected from E0771-WT (red) or E0771-GLS^KO (blue) tumors via centrifugation of harvested tumors. Glutamine (gln) was measured and concentration (μM) was calculated against a glutamine standard. Paired Student's t-test; p=0.021. n=5 mice per group. (**K**) IFNγ ELISA of supernatants collected from Tc1 CD8$^+$ T cells activated (αCD3/αCD28) in media supplemented with 0.1, 0.5, or 2 mM glutamine (n=3). Two-way ANOVA; unpaired Student's t-test. (**L-N**) E0771(OVA) sgLacZ (WT, red) or sgGls3 (GLS^KO, blue) (5x10^5) cells were bilaterally implanted into the #4 mammary fat pads of female C57BL/6 mice. (**L**) Experimental timeline is shown. (**M**) Immunofluorescence of GFP$^+$CD8$^+$ OT-I (GFP$^+$CTLs) cells in tumors. Nuclei were stained with DAPI (blue). Arrows indicate GFP$^+$CD8$^+$ OT-I T cells. Scale bar is 20 μm. (**N**) Flow cytometric analysis of of GFP$^+$CD8$^+$ T cells from whole cell tumor preparations, plotted as percentage of all live cells. Unpaired Student's t-test; p=0.043. n=3-4 mice per group. *p<0.05, **p<0.01, ***p<0.005.
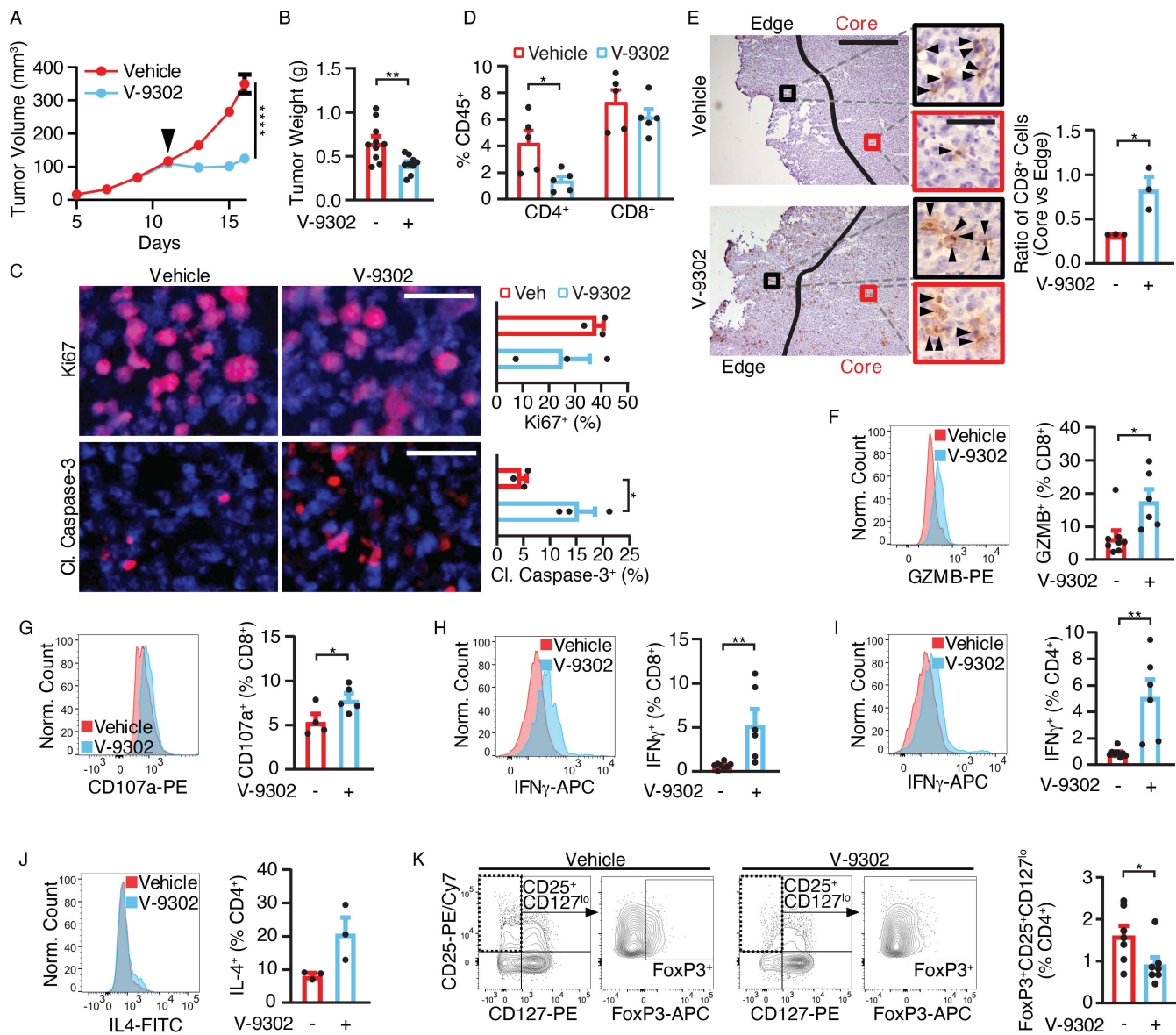
Figure 5. The glutamine transporter inhibitor V-9302 suppresses tumor growth and increases T lymphocyte activation in a model of TNBC. E0771 cells (2.5x10^5) were bi-laterally injected into the #4 mammary fat pads of female C57BL/6 mice (Taconic). Beginning at day 11, mice were treated with vehicle (DMSO, red) or 50 mg/kg V-9302 (blue) daily for 5 days. (**A**) Tumor volume was measured over time. Arrow indicates beginning of treatment. Two-way ANOVA; p<1x10^-15. n=9-10 mice per group. (**B**) Average tumor mass per mouse at harvest. Unpaired Student's t-test; p=0.0060. n=9-10 mice per group. (**C**) Immunofluorescence of tumor sections for Ki67 (top) or cleaved caspase-3 (bottom), both red. Nuclei were stained with DAPI (blue). Scale bar is 20 μm. Ki67^+, cleaved caspase-3^+, and nuclei were averaged from three fields of view. Unpaired Student's t-test; p=0.283 (Ki67), p=0.023 (Cl. Casp-3). (**D**) Flow cytometric analyses of CD4^+ (left) or CD8^+ (right) T cells, plotted as a percentage (%) of CD45^+ immune cells, in vehicle- (red) or V-9302-treated (blue) tumors. Unpaired Student's t test; p=0.023 (CD4^+), p=0.340 (CD8^+). n=5 mice per group. (**E**) Immunohistochemistry of CD8a (brown) from vehicle or V-9302-treated (50 mg/kg) tumors. Nuclei were stained with hematoxylin (blue). Edge (black) is considered <500μm (denoted by solid line) from tumor margin, core (red) is >500μm. Scale bars are 500μm and 50μm for expanded or enlarged images, respectively. CD8^+ cells (denoted by arrows) were averaged from three fields of view and normalized to field-of-view area. Unpaired Student's t-test; p=0.019. n=3 mice per group. (**F-K**) Flow cytometric analyses of (**F**) CD8^+GZMB^+, (**G**) CD8^+CD107a^+, (**H**) CD8^+IFNγ^+, (**I**) CD4^+IFNγ^+, (**J**) CD4^+IL-4^+, and (**I**) CD4^+FoxP3^+CD25^+CD127^lo CD45^+CD3^+ T cells in vehicle (red) or V-9302-treated (blue) tumors. Unpaired Student's t-test; p=0.014 (CD8^+GZMB^+), p=0.047 (CD8^+CD107a^+), p=0.007 (CD8^+IFNγ^+), p=0.0021 (CD4^+IFNγ^+), p=0.057 (CD4^+IL-4^+), p=0.034 (CD4^+FoxP3^+CD25^+CD127^lo). n=3-8 mice per group. *p<0.05, **p<0.01, ****p<0.001.
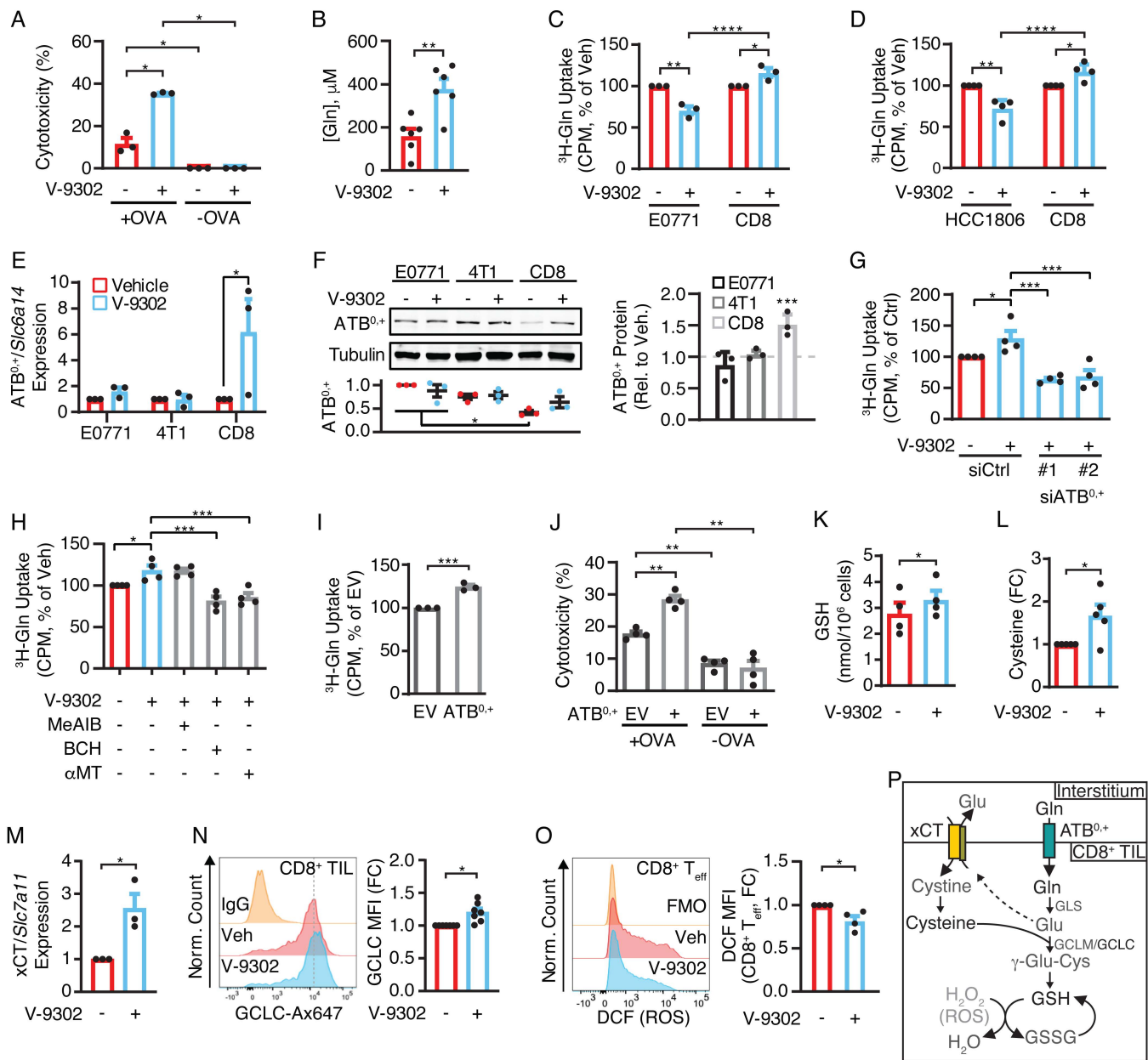
Figure 6. V-9302 induces ATB$^{0,+}$ expression to sustain glutamine uptake and glutathione synthesis in activated CD8$^+$ T cells. (**A**) LDH cytotoxicity of E0771(OVA) and CD8$^+$ OT-I CTLs co-cultured in vehicle (red) or V-9302 (blue) (n=3). One-way ANOVA (p=0.0018), Tukey's post-hoc. (**B**) Tumor interstitial fluid glutamine in vehicle or V-9302-treated tumors. Unpaired Student's t-test; p=0.0027. n=6 mice per group. (**C-D**) ^{3}H-glutamine uptake assay in (**C**) E0771 and C567BL/6 CD8$^+$ CTLs or (**D**) HCC1806 and human CD8$^+$ CTLs isolated from PBMCs in vehicle or V-9302 (n=3-4). Averaged triplicate radioactivity (CPM) was normalized to vehicle. Two-way ANOVA (E0771: p=2.18x10^{-4}; HCC1806: p=1.43x10^{-4}), Tukey's post-hoc. (**E**) Relative expression of ATB$^{0,+}$/*Slc6a14* (n=3). Two-way ANOVA (p=0.036), Tukey's post-hoc. (**F**) ATB$^{0,+}$ western blot of cells from (*E*). Relative ATB$^{0,+}$ protein was normalized as indicated (n=3). Two-way ANOVA (bottom, p=0.0014; right, p=0.0026), Tukey's (bottom) or Sidak's (right) post-hoc. (**G-H**) ^{3}H-glutamine uptake of CD8$^+$ CTLs (**G**) after *ATB$^{0,+}$* knockdown or (**H**) in the presence of glutamine transporter inhibitors, as indicated (n=4). One-way ANOVA ((G): p=4.98x10^{-5}; (H): p=3.41x10^{-4}), Holm-Sidak post-hoc. (**I-J**) CD8$^+$ CTLs overexpressing ATB$^{0,+}$ were evaluated for (**I**) ^{3}H-glutamine uptake or (**J**) LDH cytotoxicity (n=3-4). Empty vector (EV) was used as a control. (*I*) Unpaired Student's t-test (p=7.39x10^{-4}). (*J*) One-way ANOVA (p=4.13x10^{-5}), Tukey's post-hoc. (**K-L**) Intracellular (**K**) GSH and (**L**) cysteine in CD8$^+$ CTLs (n=4-5). Paired (p=0.020) (*K*) or unpaired (p=0.027) (*L*) Student's t-test. (**M**) xCT/*Slc7a11* expression in activated CD8$^+$ CTLs (n=3). Unpaired Student's t-test, p=0.025. (**N**) GCLC protein expression in CD8$^+$ TILs in tumors of vehicle or V-9302-treated mice. Dotted line denotes vehicle peak in representative data shown. Unpaired Student's t-test, p=0.0034. n=7 mice per group. (**O**) ROS in activated CD8$^+$CD44$^+$CD62L$^-$ effector T cells by DCF (n=4). Unpaired Student's t-test, p=0.016. (**P**) Proposed model of V-9302-mediated increases (bold) and decreases (gray) in CD8$^+$ TILs. *p<0.05, **p<0.01, ***p<0.005, ****p<0.001.